Experimental and Numerical Investigation on Large Deformation Reconstruction of Thin Laminated Composite Structures using Inverse Finite Element Method

M.A. Abdollahzadeh[1,2,3], H.Q. Ali[1,2,3], M. Yildiz[1,2,3], A. Kefal[1,2,3],*

[1]*Faculty of Engineering and Natural Sciences, Sabanci University, Tuzla, Istanbul 34956, Turkey*
[2]*Integrated Manufacturing Technologies Research and Application Center, Sabanci University, Tuzla, Istanbul 34956, Turkey*
[3]*Composite Technologies Center of Excellence, Istanbul Technology Development Zone, Sabanci University-Kordsa Global, Pendik, Istanbul 34906, Turkey*
*Corresponding author: adnankefal@sabanciuniv.edu

Abstract: The inverse finite element method (iFEM) is one of the best candidates to perform displacement monitoring (shape sensing) of structures using a set of on-board/embedded strain sensors. This study demonstrates the high efficiency, robustness, and accuracy of the iFEM approach to reconstruct geometrically non-linear deformations of thin laminated plates and shells by performing experimental measurements and numerical analyses. The iFEM formulation is derived based on the first-order shear deformation theory of plates. A weighted least-squares variational principle is utilized with incremental non-linear strains while performing the geometrical update of the model using predicted incremental deformations. Moreover, a quadrilateral inverse-shell element (iQS4) is employed to discretize the whole domain of the laminated panels and solve the numerical/experimental shape-sensing problems. Further, a polynomial strain pre-extrapolation technique is incorporated with the iQS4 formulation to smoothen the discrete strain data obtained from a few strain rosettes placed along the entire length of the structures. For each case study, a high-fidelity finite element analysis is performed to establish a reference displacement solution. Finally, the qualitative and quantitative comparison of reconstructed displacement results with reference solutions confirms the superior potential of the iFEM-iQS4 approach for full-field shape sensing of thin laminates undergoing non-linear deformations.

Keywords: Thin laminated composites, large displacement, inverse finite element method, nonlinear strain measurement, structural health monitoring.

1

1. Introduction

Long fiber-reinforced polymer composites with advanced mechanical performances are commonly used to manufacture laminated structures of two or more plies with variable fiber angles to offer high flexural rigidity and lighter weight. These laminated structures can be classified according to their span-to-thickness ratio ρ as thin (slender), $\rho \geq 100$, moderately thick, $10 \leq \rho \leq 100$, and thick plates or shells, $\rho \leq 10$ [1]. Among this class of composites, thin laminated plates are widely used for various types of aerospace, marine, and civil structures due to their improved mechanical properties, i.e., long fatigue life [2-3], high strength [4-5], and superior corrosion resistance [6]. However, the thin laminated structures are susceptible to geometrically non-linear displacements due to harsh operating conditions, such as large deflections and/or buckling deformations. Therefore, the safety of these structures must be ensured by a reliable inspection system in real time. To this end, structural health monitoring (SHM) systems can be effectively employed to dynamically track large structural deformations for predicting any occurrence of progressive damage accumulation before catastrophic structural failure. For instance, in the last few decades, various SHM techniques have been used to detect damage and failure modes of composite structures utilizing embedded and/or surface-mounted sensor systems [7-10]. Hence, smart composites integrated with sensors and SHM systems is key to future engineering science and technology.

Shape sensing is one of the critical aspects of SHM systems that deals with the real-time reconstruction of deformation levels on structural components [11]. This approach utilizes experimental strain data collected from a network of on-board/embedded sensors which can be transmitted via wireless or wired (conventional) techniques to data processing platforms. Fiber Bragg Grating (FBG) sensors and strain rosettes are among the wired systems primarily used in composite structures due to their simple and efficient applicability. FBG sensors are flexible and durable enough to embed in composite materials easily [12]. When these sensors are embedded in the laminated structure, they can observe temporary and permanent strain variations at discrete positions within the composite materials [13-14]. Shape sensing is an inverse problem. Inverse problems arise in a variety of sensing applications. Recently, data-driven methods using neural networks have been shown to be significantly superior to classical solution methods for inverse problems [15]. Surrogate modelling was also created to speed up the solution of the inverse problems [16]. To obtain a solution for a full-field displacement, in situ sensor measurements must

be used in an inverse method to solve the shape sensing problem. To this end, several inverse methods such as modal [17-19], analytical [20], and curve-fitting [21] approaches have been proposed in the literature. The inverse finite element method is a state-of-the-art robust shape-sensing algorithm [22-23] that has recently attracted much more attention than other inverse methods due to its unique features. These advantages mainly include (i) no requirement of loading/material information and (ii) full-field deformation reconstruction capability over the entire structural domain.

The iFEM method was initially developed based on the first-order shear deformation theory (FSDT) for the shape estimation of plate structures. The critical input of this method is triaxial strain data obtained from a discrete number of on-board sensors, e.g., strain rosettes. The iFEM algorithm minimizes the difference between the calculated numerical strains and their experimental counterparts utilizing a weighted least-squares functional. Thus far, different types of the inverse beam [24-25] and plate/shell [26-27] elements have been proposed using iFEM methodology for real-time monitoring of complex deformed shapes. In a recent comparative study, the performance of C^0-continuous inverse shell elements was investigated for shape sensing and damage detection of various plate/shell-like geometries [29]. Furthermore, experimental and numerical studies leveraged the iFEM algorithm for displacement and stress monitoring of different marine [30-34], aerospace [35-38], and civil structures [39-41]. Also, recent research efforts have addressed the optimal placement of sensors for iFEM analyses using effective optimization methods [42-44].

Additionally, isogeometric iFEM formulations were developed for displacement monitoring of thin-shell [45-46] and beam-like [47-48] structures. Most recently, Kefal et al. [49] have introduced coupling of iFEM methodology with a nonlocal meshless approach known as peridynamics for crack propagation monitoring of laminated composite plates. Besides, the ability of the iFEM approach was numerically demonstrated for shape sensing of isotropic plates undergoing large deformations [50]. Since the FSDT-based iFEM method may not always be applicable to accurate reconstruction of the displacement, strain, and stress fields of thick multi-layered composite and sandwich structures, enhanced iFEM formulations [51-52] were developed by extending kinematic relations towards zigzag theories [53]. On this basis, smoothed iFEM approach has been proposed by coupling enhanced iFEM formulation with smoothing element

3

analysis for effective shape sensing application [54]. The predictive capability of the enhanced iFEM approaches was numerically and experimentally assessed on real-time displacement monitoring of moderately thick sandwich structures [55-56]. In addition to top/bottom sensor, these iFEM formulations require an additional set of interlaminar in-situ strain data (which can be obtained from embedded FBG sensors) for thick structures. Therefore, the iFEM-FSDT formulation is preferable compared to enhanced iFEM methods in terms of practical experimental implementation on thin-walled structures with a smaller number of strain sensors.

Real-time deformation prediction of thin laminated plates/shells plays a critical role in the realistic assessment of structural damage and fatigue life of structural components used in today's engineering industry. In this regard, the need for an extensive numerical-experimental application of iFEM-FSDT to thin-walled composite structures is evident. Nevertheless, the predictive capability of the iFEM algorithm has not been assessed for reconstructing geometrical nonlinear deformations of thin composite structures subjected to bending and/or post-buckling loads. Among the myriad of computational or experimental shape-sensing investigations, the application of iFEM-FSDT to displacement monitoring of composites is limited to only a few studies, which include linear elastic shape-sensing of thin composite structures under thermo-mechanical [57], compressive linear-buckling [58], and impact [59] loads.

To fill the critical gap mentioned above, this study performs geometrically nonlinear deformation reconstruction of thin composite plates and shells using experimental strain measurements employing iFEM-FSDT formulation for the first time. Therefore, the novelty of this study lies in the numerical and experimental investigation of the iFEM-FSDT approach for shape sensing of thin laminated structures undergoing large bending/post-buckling deflections in real time. For this purpose, two numerical and one experimental study cases are performed to verify the iFEM approach for nonlinear shape sensing of thin laminates. A robust and computationally efficient quadrilateral inverse shell element (iQS4) [27] is used to perform the nonlinear iFEM analysis. In addition, the iFEM-iQS4 model is extended through a smoothing analysis to recover continuous strains from discrete strain measurements obtained during the experimental test. Finally, the obtained iFEM results are validated by the reference solutions generated using a well-known commercial finite element software, i.e., ANSYS APDL.

This paper is organized in the following order. In Section 2, the fundamental formulation of the iQS4 element, the algorithm of nonlinear-displacement geometric update, and the polynomial smoothing approach are summarized. Section 3 first describes the numerical examples, (1) a post-buckling analysis of a thin laminated plate and (2) bending analysis of a curved plate with large deflection using the iFEM technique. Then, experimental shape-sensing implementation of iFEM-iQS4 for thin laminated plate is elaborated in Section 3. Finally, in Section 4, several important implications are drawn from the iFEM results of the thin multi-layered composite structures exposed to large bending/buckling deformations.

2. Theoretical Framework

2.1 The iFEM-iQS4 Element for Shape Sensing of Thin Laminated Structures

The iQS4 is an inverse shell element with four nodes, originally developed by Kefal et al. [25], for shape and stress sensing of plate/shell structures. Each node of this inverse element has three translational (v_{1i}, v_{2i}, v_{zi}) and three rotational (θ_{1i}, θ_{2i}, θ_{zi}) degrees of freedom (DOF) with the positive directions as shown in Fig. 1(a). With the use of hierarchical drilling rotation DOF, θ_{zi}, this element becomes a robust iFEM tool for modelling curved/blade-stiffened shell geometries. Mathematical fundamentals for the development of the elements with drilling DOF were investigated in detail by Hughes and Brezzi [60].
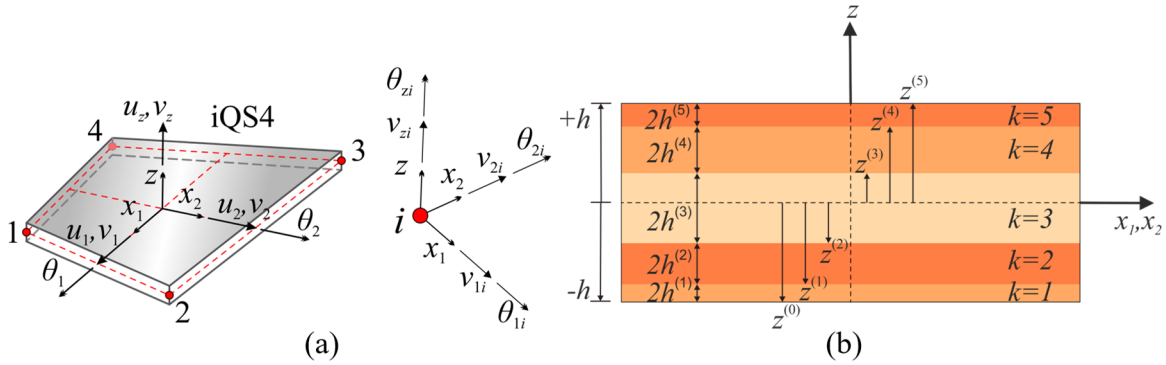
Fig. 1. (a) Geometry of iQS4 inverse shell element with associated coordinates and its nodal DOFs, (b) Cross-section of a laminated panel.

The element has a total thickness of *2h*, and therefore its thickness coordinate is defined as $z \in (-h, +h)$. Besides, the element is oriented with respect to a local (element) coordinate system, $\mathbf{x} \equiv (x_1, x_2)$, representing the in-plane coordinates of the element. Here, the iQS4 element is

employed to model a laminate with a total number of n_L layers (made of isotropic or orthotropic materials) as shown in Fig. 1(b). The laminate notation can be described as follows. The superscript (k) is utilized to identify the interlaminar strain field and thickness coordinate between $(k-1)$-th and k-th plies. Besides, the (k)-th lamina has thickness of $2h^{(k)}$ with the top and bottom thickness coordinates, $z^{(k-1)}$ and $z^{(k)}$, respectively, as illustrated in Fig. 1(b).

Regardless of the individual ply kinematics, the in-plane and out-of-plane displacement components of any material point can be described according to FSDT as a function of five independent kinematic variables as:

$$u_1(\mathbf{x}, z) = v_1(\mathbf{x}) + z\theta_2(\mathbf{x}) \tag{1}$$

$$u_2(\mathbf{x}, z) = v_2(\mathbf{x}) - z\theta_1(\mathbf{x}) \tag{2}$$

$$u_z(\mathbf{x}, z) = v_z(\mathbf{x}) \tag{3}$$

where translational (v_1, v_2, v_z) and rotational (θ_1, θ_2) kinematic variables can be approximated utilizing shape functions of the iQS4 element as [27]:

$$v_1(\mathbf{x}) = \sum_{i=1}^{4} \left(N_i v_{1i} + L_i \theta_{zi} \right) \tag{4}$$

$$v_2(\mathbf{x}) = \sum_{i=1}^{4} \left(N_i v_{2i} + M_i \theta_{zi} \right) \tag{5}$$

$$v_z(\mathbf{x}) = \sum_{i=1}^{4} \left(N_i v_{zi} - L_i \theta_{1i} - M_i \theta_{2i} \right) \tag{6}$$

$$\theta_i(\mathbf{x}) = \sum_{j=1}^{4} N_j \theta_{ij} \quad (i = 1, 2) \tag{7}$$

where the isoparametric mapping of in-plane coordinates to parent domain (s, t) can be performed using the nodal coordinates of the iQS4 element, x_{1i}, x_{2i} $(i = 1, 2, 3, 4)$, as:

$$\mathbf{x} = \begin{Bmatrix} x_1(s,t) \\ x_2(s,t) \end{Bmatrix} = \sum_{i=1}^{4} N_i \begin{Bmatrix} x_{1i} \\ x_{2i} \end{Bmatrix} \tag{8}$$

In Eqs. (4-7), the $L_i \equiv L_i(s,t)$ and $M_i \equiv M_i(s,t)$ functions are the second order anisoparametric shape functions [58], and $N_i \equiv N_i(s,t)$ is bilinear isoparametric shape functions. The explicit form of these shape functions can be found in references [27, 61].

Substituting Eqs. (4-7) to Eqs. (1-3) and subsequently taking the spatial derivatives of the resultant displacement vector according to infinitesimal strain theory, the in-plane, $\boldsymbol{\varepsilon}$, and transverse-shear, $\boldsymbol{\gamma}$, strains at every position of the plate/shell domain can be derived analytically in terms of the nodal DOF vector of the iQS4 element, $\mathbf{u}^e$, as:

$$\boldsymbol{\varepsilon}(\mathbf{u}^e) = \mathbf{e}(\mathbf{u}^e) + z\boldsymbol{\kappa}(\mathbf{u}^e) = (\mathbf{B}^e + z\mathbf{B}^\kappa)\mathbf{u}^e \tag{9}$$

$$\boldsymbol{\gamma}(\mathbf{u}^e) = \mathbf{B}^\gamma \mathbf{u}^e \tag{10}$$

$$\mathbf{u}^e = \begin{bmatrix} \mathbf{u}_1^e & \mathbf{u}_2^e & \mathbf{u}_3^e & \mathbf{u}_4^e \end{bmatrix}^T \tag{11}$$

$$\mathbf{u}_i^e = \begin{bmatrix} v_{1i} & v_{2i} & v_{zi} & \theta_{1i} & \theta_{2i} & \theta_{zi} \end{bmatrix} \quad (i=1,2,3,4) \tag{12}$$

where $\mathbf{u}_i^e$ represents the DOF of the i-th node, the $\mathbf{e}(\mathbf{u}^e)$ and $\boldsymbol{\kappa}(\mathbf{u}^e)$ vectors are the membrane and bending section strains, respectively, and the $\mathbf{B}^\chi = \begin{bmatrix} \mathbf{B}_1^\chi & \mathbf{B}_2^\chi & \mathbf{B}_3^\chi & \mathbf{B}_4^\chi \end{bmatrix}$ $(\chi = e, \kappa, \gamma)$ matrices are the strain-displacement matrices of the iQS4 element. These matrices contain derivatives of the shape functions with respect to x_1 and x_2 axes and can be explicitly described as [27]:

$$\mathbf{B}_i^e \equiv \begin{bmatrix} N_{i,1} & 0 & 0 & 0 & 0 & L_{i,1} \\ 0 & N_{i,2} & 0 & 0 & 0 & M_{i,2} \\ N_{i,2} & N_{i,1} & 0 & 0 & 0 & L_{i,2} + M_{i,1} \end{bmatrix} \quad (i=1,2,3,4) \tag{13}$$

$$\mathbf{B}_i^\kappa \equiv \begin{bmatrix} 0 & 0 & 0 & 0 & N_{i,1} & 0 \\ 0 & 0 & 0 & -N_{i,2} & 0 & 0 \\ 0 & 0 & 0 & -N_{i,1} & N_{i,2} & 0 \end{bmatrix} \quad (i=1,2,3,4) \tag{14}$$

$$\mathbf{B}_i^\gamma \equiv \begin{bmatrix} 0 & 0 & N_{i,1} & -L_{i,1} & -M_{i,1} + N_i & 0 \\ 0 & 0 & N_{i,2} & -L_{i,2} - N_i & -M_{i,2} & 0 \end{bmatrix} \quad (i=1,2,3,4) \tag{15}$$

where the comma subscript followed by 1 and 2 indicates the partial derivative of $(\cdot)_{,\alpha} = \frac{\partial(\cdot)}{\partial x_\alpha}$ $(\alpha = 1,2)$. Using the chain rule and the inverse of the Jacobian matrix of the iQS4 element, one can calculate the derivatives of the shape functions, $N_{i,j}, L_{i,j}, M_{i,j}$ $(j=1,2)$, as:

$$\begin{Bmatrix} \chi_{i,1} \\ \chi_{i,2} \end{Bmatrix} = \begin{bmatrix} x_{1,s} & x_{2,s} \\ x_{1,t} & x_{2,t} \end{bmatrix}^{-1} \begin{Bmatrix} \chi_{i,s} \\ \chi_{i,t} \end{Bmatrix} \quad (\chi = N, L, M) \tag{16}$$

7

where the symbol $(\cdot)_{,\alpha} = \frac{\partial(\cdot)}{\partial\alpha}$ $(\alpha = s,t)$ indicates the partial derivatives of the shape functions or local in-plane coordinates with respect to the isoparametric coordinates.

The experimental surface strains collected from the on-board strain rosettes and/or embedded FBG sensors are the main input of the iFEM-iQS4 formulation. To provide this data, the sensors must be located in at least two different positions along the thickness coordinate of the laminate for a given discrete in-plane position, $\mathbf{x}_i \equiv (x_1, x_2)_i$ $(i = 1, 2, ..., n_S)$, where the n_S represents the number of the two strain rosettes set. For clarity, an example of sensor placement configuration is depicted in Fig. 2, where $\boldsymbol{\varepsilon}_i^{(\chi)}$ $(\chi = k_1, k_2)$ denotes the interlaminar triaxial strains measured at k_1 and k_2 interface of the plies at $\mathbf{x}_i$ position. Here, $k_i \in [0, n_L]$ $(i = 1, 2)$ interfaces can be assigned to any arbitrarily integer and it is assumed that k_2 interface is closer to the top surface of the laminate than k_1 interface as such $k_2 > k_1$.
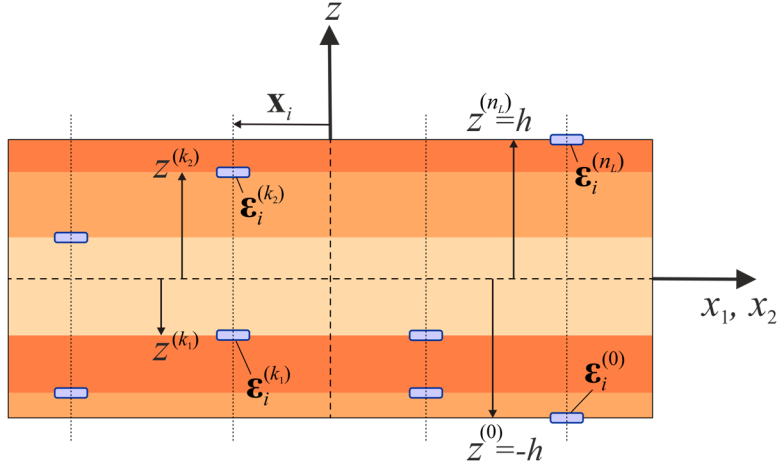
Fig. 2. Layout of strain sensors along the thickness coordinate of the thin laminated composite structure.

Utilizing the in-plane strain definition given in Eq. (9), experimental surface strains, $\boldsymbol{\varepsilon}_i^{(k_1)}$ and $\boldsymbol{\varepsilon}_i^{(k_2)}$, can be expressed in terms of the experimental membrane, $\mathbf{e}^\varepsilon$, and bending, $\boldsymbol{\kappa}^\varepsilon$, section strains as:

$$\boldsymbol{\varepsilon}_i^{(k_1)} \equiv \boldsymbol{\varepsilon}(\mathbf{x}_i, z^{(k_1)}) = \mathbf{e}^\varepsilon(\mathbf{x}_i) + z^{(k_1)}\boldsymbol{\kappa}^\varepsilon(\mathbf{x}_i) \tag{17}$$

$$\boldsymbol{\varepsilon}_i^{(k_2)} \equiv \boldsymbol{\varepsilon}(\mathbf{x}_i, z^{(k_2)}) = \mathbf{e}^\varepsilon(\mathbf{x}_i) + z^{(k_2)}\boldsymbol{\kappa}^\varepsilon(\mathbf{x}_i) \tag{18}$$

which be solved to obtained general description of experimental membrane and bending section strains of laminate with n_L plies as:

$$\mathbf{e}^{\varepsilon}(\mathbf{x}_i) \equiv \mathbf{e}_i^{\varepsilon} = \frac{\boldsymbol{\varepsilon}_i^{(k_1)} z^{(k_2)} - \boldsymbol{\varepsilon}_i^{(k_2)} z^{(k_1)}}{\displaystyle\sum_{k=k_1+1}^{k_2} 2h^{(k)}} \quad (i=1,2,...,n_S; \, k_2 > k_1) \tag{19}$$

$$\boldsymbol{\kappa}^{\varepsilon}(\mathbf{x}_i) \equiv \boldsymbol{\kappa}_i^{\varepsilon} = \frac{\boldsymbol{\varepsilon}_i^{(k_2)} - \boldsymbol{\varepsilon}_i^{(k_1)}}{\displaystyle\sum_{k=k_1+1}^{k_2} 2h^{(k)}} \quad (i=1,2,...,n_S; \, k_2 > k_1) \tag{20}$$

It is important to recall that the $\mathbf{e}_i^{\varepsilon}$ and $\boldsymbol{\kappa}_i^{\varepsilon}$ vectors are the experimental counterparts of the membrane, $\mathbf{e}(\mathbf{u}^e)$, and bending, $\boldsymbol{\kappa}(\mathbf{u}^e)$, section strains given in Eq. (9), and thus can be directly computed during the experimental test given that the $\boldsymbol{\varepsilon}_i^{(k_1)}$ and $\boldsymbol{\varepsilon}_i^{(k_2)}$ are gathered by sensors. If no experimental test is available, these strain measurements can be simulated using numerical methods such as finite element method to be able to optimize sensor placement configurations for an experimental setup. If surface mounted strain gauges are located on top and bottom position of the laminate (i.e., no embedded FBG sensors), the interface indices are automatically set to $k_1 = 0; \, k_2 = n_L$ in Eqs. (19-20), leading to the original expression of the iFEM-iQS4 formulation for isotropic plates/shells as [22]:

$$\mathbf{e}_i^{\varepsilon} = \frac{\boldsymbol{\varepsilon}_i^{(0)} z^{(n_L)} - \boldsymbol{\varepsilon}_i^{(n_L)} z^{(0)}}{\displaystyle\sum_{k=1}^{n_L} 2h^{(k)}} = \frac{\boldsymbol{\varepsilon}_i^{(0)} h - \boldsymbol{\varepsilon}_i^{(n_L)}(-h)}{2h} = \frac{\boldsymbol{\varepsilon}_i^{(0)} + \boldsymbol{\varepsilon}_i^{(n_L)}}{2} \tag{21}$$

$$\boldsymbol{\kappa}_i^{\varepsilon} = \frac{\boldsymbol{\varepsilon}_i^{(n_L)} - \boldsymbol{\varepsilon}_i^{(0)}}{\displaystyle\sum_{k=1}^{n_L} 2h^{(k)}} = \frac{\boldsymbol{\varepsilon}_i^{(n_L)} - \boldsymbol{\varepsilon}_i^{(0)}}{2h} \tag{22}$$

where the vectors $\boldsymbol{\varepsilon}_i^{(n_L)}, \boldsymbol{\varepsilon}_i^{(0)}$ represent the top and bottom surface triaxial strains collected from sensors at any $\mathbf{x}_i$ position (Fig. 2). Unlike the membrane and bending section strains, experimental counterpart of the transverse-shear strains $\boldsymbol{\gamma}(\mathbf{u}^e)$ cannot be extracted directly using surface strain data, $\boldsymbol{\varepsilon}_i^{(\chi)}$ ($\chi = k_1, k_2$). However, the contributions of transverse-shear strains to large bending deformations can be ignored for shape sensing of thin-walled structures.

For an individual iQS4 element with the area of A^e, the weighted least-squares functional of iFEM methodology can be expressed based on calculated errors between analytical and experimental section strains as [23, 27]:

$$\Phi(\mathbf{u}^e) = \frac{1}{A^e} \iint_{A^e} \left(w_e \left\| \mathbf{e}(\mathbf{u}^e) - \mathbf{e}^\varepsilon \right\|^2 + w_\kappa (2h)^2 \left\| \mathbf{\kappa}(\mathbf{u}^e) - \mathbf{\kappa}^\varepsilon \right\|^2 + w_\gamma \left\| \mathbf{\gamma}(\mathbf{u}^e) \right\|^2 \right) dx_1 dx_2 \tag{23}$$

where the w_e and w_κ represent the weighting constants related to the membrane and bending strains respectively, and w_γ stands for the weighting coefficient of transverse-shear strains that is always set to a small number compared to unity, e.g., $w_\gamma = 10^{-5}$, due to the lack of experimental counterpart. In the case of $\mathbf{e}^\varepsilon$ and $\mathbf{\kappa}^\varepsilon$ section strains being available for the iQS4 element, the weighting coefficients take the value of unity ($w_e = w_\kappa = 1$). Otherwise, they should be set to relatively small values such as $w_e = w_\kappa = 10^{-5}$. Minimizing the $\Phi(\mathbf{u}^e)$ functional with respect to the unknown $\mathbf{u}^e$ nodal displacement of the iQS4 element, the final equation system of the element can be written as:

$$\frac{\partial \Phi(\mathbf{u}^e)}{\partial \mathbf{u}^e} = 0 \implies \mathbf{k}^e \mathbf{u}^e = \mathbf{f}^e \tag{24}$$

$$\mathbf{k}^e = \frac{1}{A^e} \iint_{A^e} \left(w_e (\mathbf{B}^e)^T \mathbf{B}^e + w_\kappa (2h)^2 (\mathbf{B}^\kappa)^T \mathbf{B}^\kappa + w_\gamma (\mathbf{B}^\gamma)^T \mathbf{B}^\gamma \right) dx_1 dx_2 \tag{25}$$

$$\mathbf{f}^e = \frac{1}{A^e} \iint_{A^e} \left(w_e (\mathbf{B}^e)^T \mathbf{e}^\varepsilon + w_\kappa (2h)^2 (\mathbf{B}^\kappa)^T \mathbf{\kappa}^\varepsilon \right) dx_1 dx_2 \tag{26}$$

where the $\mathbf{k}^e$ and $\mathbf{f}^e$ indicate shape matrix and experimental strain vectors corresponding to an individual element in the given order. Note that, unlike shape matrix $\mathbf{k}^e$, the $\mathbf{f}^e$ vector is dependent on experimental measurements. To numerically compute the area integral in Eq. (26), the discrete values of the experimental section strains, $\mathbf{e}_i^\varepsilon$ and $\mathbf{\kappa}_i^\varepsilon$, given by Eqs. (21-22) are required at the Gauss points of the iQS4 element. One can employ 'a priori' strain smoothing methods or "smoothed iFEM" to overcome this issue for practical applications [54]. Alternatively, if a single sensor set is available within the iQS4 element, then the experimental data can be assigned uniformly to each Gauss integration point (e.g., the same $\mathbf{e}_i^\varepsilon$ and $\mathbf{\kappa}_i^\varepsilon$ values for each of four Gauss points). For reasonable averaging of the sensor data, the centroid element can be chosen to mount

this sensor set [28]. A suitable transformation matrix, $\mathbf{T}^e$, should be utilized to transform the iFEM equation (Eq. 24) from local to global coordinate system, and then they can be assembled for the entire iQS4 discretization as:

$$\mathbf{KU} = \mathbf{F} \tag{27}$$

$$\mathbf{K} = \bigcup_{e=1}^{n_{el}} \left((\mathbf{T}^e)^T \mathbf{k}^e \mathbf{T}^e \right) \tag{28}$$

$$\mathbf{F} = \bigcup_{e=1}^{n_{el}} \left((\mathbf{T}^e)^T \mathbf{f}^e \right) \tag{29}$$

$$\mathbf{U} = \bigcup_{e=1}^{n_{el}} \left((\mathbf{T}^e)^T \mathbf{u}^e \right) \tag{30}$$

where n_{el} denotes the number of inverse elements for a given discretization, and the $\bigcup$ operator represents the finite element assembly process. The details of computing the $\mathbf{T}^e$ transformation matrix by using global coordinates of the nodes were given in reference [28]. In Eq. (27), the $\mathbf{K}$, $\mathbf{U}$, and $\mathbf{F}$ symbols are referred to global shape matrix, displacement vector and experimental strain vector, respectively. Note that since $\mathbf{F}$ vector is dependent on experimental strain data, it needs to be updated at each time step to provide a real-time monitoring system. After imposing displacement and loading boundary conditions, the Eq. (27) can be updated for the reduced forms of global equations. Then, an inversion process is performed to solve this equation system as:

$$\mathbf{K}_R \mathbf{U}_R = \mathbf{F}_R \quad \Rightarrow \quad \mathbf{U}_R = \mathbf{K}_R^{-1} \mathbf{F}_R \tag{31}$$

which provides the real-time deformations (nodal DOF of the entire iQS4 model) for any strain increment. To obtain more accurate non-linear large deformations reconstruction for a given strain increment step, ls, the global displacement vector of the nodes, $\mathbf{U}_i \equiv \begin{bmatrix} U_i & V_i & W_i \end{bmatrix}^T$ ($i = 1, 2, ..., n_{node}$), can be utilized to update the geometry of the iFEM-iQS4 domain before the shape analysis for next strain-increment step, $ls+1$, as:

$$(\mathbf{X}_i)_{ls+1} = (\mathbf{X}_i)_{ls} + (\mathbf{U}_i)_{ls} \quad (ls = 1, 2, ..., n_{step}; i = 1, 2, 3, ..., n_{node}) \tag{32}$$

where the vector $(\mathbf{X}_i)_{ls} \equiv \begin{bmatrix} X_i & Y_i & Z_i \end{bmatrix}_{ls}^T$ indicates the global coordinates of the i-th node at strain increment step of ls, the n_{node} and n_{step} symbols stand for the total number of nodes and strain-

acquisition step. Note that the $(\mathbf{U}_i)_{ls}$ displacements are calculated by performing linear iFEM analysis. Nonlinear deformation reconstruction is enforced by using new geometrical surface, $(\mathbf{X}_i)_{ls+1}$, for the next iFEM analysis. Besides, the nonlinear deformations can be calculated correctly since the experimental section strains vary nonlinearly in case of large displacement event. If the incremental deformations are not large enough as compared to geometrical dimensions of the iQS4 model, they can be neglected for next steps. Accurate large deformation can still be monitored in this case due to the nonlinear input of experimental data. For further details of the incremental iFEM analysis, the reader can refer to the reference [50]. To facilitate the computer implementation, the flowchart and pseudocode of the iFEM-iQS4 approach have been scrutinized in Fig. 3 and Algorithm 1, respectively.
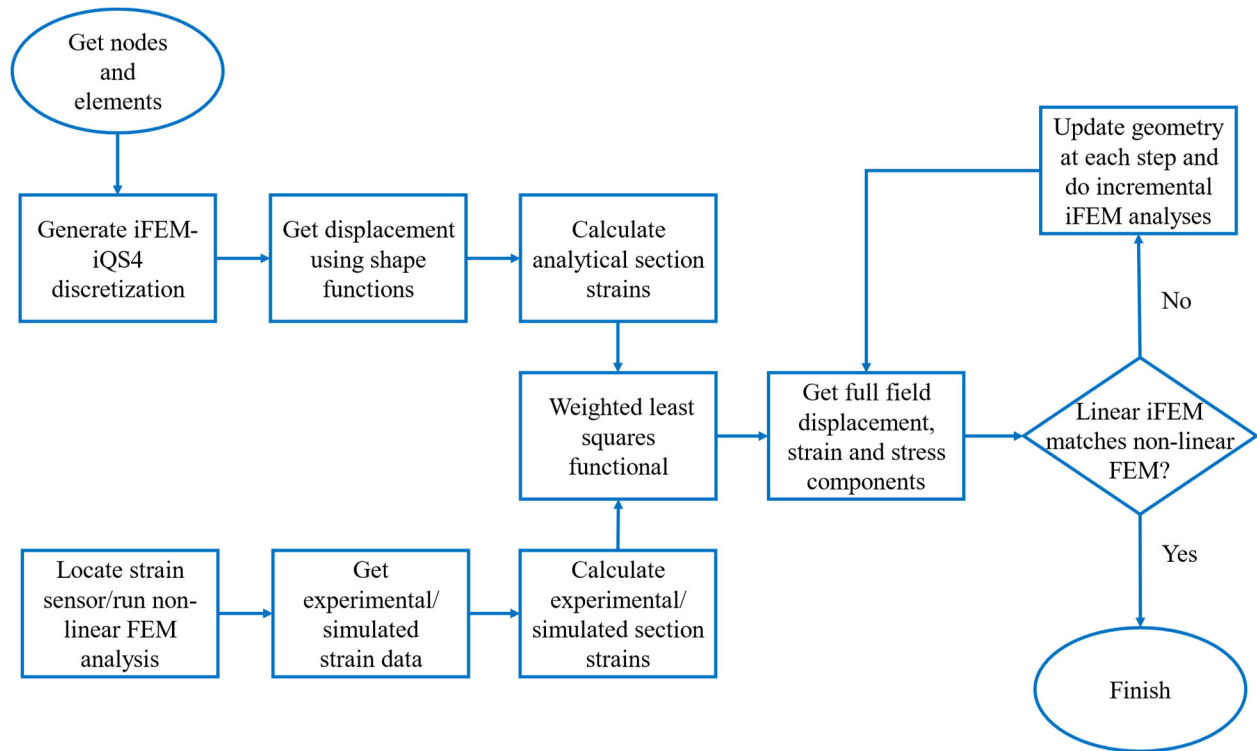
Fig. 3. Flowchart of iFEM solution for geometrically non-linear deformations.

Algorithm 1 iFEM analysis for displacement reconstruction of non-linear deformations
➢ **procedure** iFEM SOLUTION
➢ Read nodal coordinates and elements connectivity data
for $e = 1$ to n_{el} **do**
➢ Compute $\mathbf{B}^{\chi}(\chi = e, \kappa, \gamma)$ matrix defined in Eqs. (13-15)
➢ Compute $\mathbf{f}^{e}$ and $\mathbf{k}^{e}$ matrix using Eqs. (25-26)
➢ Assemble $\mathbf{f}^{e}$ and $\mathbf{k}^{e}$ matrices for all inverse elements
end
➢ Read constraint boundary conditions
➢ Compute $\mathbf{F}_{R}$ and $\mathbf{K}_{R}$ reduced matrices using constraint conditions and obtain $\mathbf{U}_{R}$
for $e = 1$ to n_{el} **do**
➢ Compute the kinematic variables using element DOF vector
➢ Compute full-field strain components
➢ Compute full-field stress components
end
if the reconstructed results are far from the reference solution
➢ Update the geometry of the structure using Eq. (32) for each time step and repeat the process until the result matches the FEM solution
end

2.2. The Role of Strain Pre-extrapolation Technique for iFEM Analysis

The experimental strain measurements are most likely noisy and erroneous, either due to operator error or poor equipment. In addition, due to the tendency to use a minimum number of sensors in real conditions, the number of sensors is optimally chosen, which can lead to discontinuity between strain data. To minimize this type of errors and to obtain a continuous distribution of experimental strains over the entire area of the plate, the experimental strain data can be processed using analytical techniques. Different types of smoothing techniques for stress and strain recovery and error estimating have been discussed in the literature [62-63]. Strain pre-extrapolation is one of those techniques which is based on data smoothing. To implement the proposed methodology for the experimental example, the number of sensors is kept constant while a high-resolution iFEM mesh is used to generate additional elements throughout the domain. A multinomial curve is then fitted through the available discrete experimental strain measurement points to replace the missing strain values with virtual strain data. The least squares method is a curve fitting technique which fits polynomials through discretely determined strain data. The general form of a polynomial with *k*-th order takes the form:

$$\varepsilon(\xi) = \alpha_k \xi^k + \cdots + \alpha_2 \xi^2 + \alpha_1 \xi + \alpha_0 \tag{33}$$

where α_i $(i = 0, 1, 2, ..., k)$ is the polynomial coefficient and the term k is the degree of the polynomial curve. The least-squares method minimizes the difference between the estimated values of the polynomial and the expected values from the data set. The coefficients of the polynomial regression model are determined by solving system of linear equations as follows:

$$\begin{bmatrix} n_P & \sum_{i=1}^{n_P} \xi_i & \cdots & \sum_{i=1}^{n_P} \xi_i^k \\ \sum_{i=1}^{n_P} \xi_i & \sum_{i=1}^{n_P} \xi_i^2 & \cdots & \sum_{i=1}^{n_P} \xi_i^{k+1} \\ \vdots & \vdots & \ddots & \vdots \\ \sum_{i=1}^{n_P} \xi_i^k & \sum_{i=1}^{n_P} \xi_i^{k+1} & \cdots & \sum_{i=1}^{n_P} \xi_i^{2k} \end{bmatrix} \begin{Bmatrix} \alpha_0 \\ \alpha_0 \\ \vdots \\ \alpha_k \end{Bmatrix} = \begin{Bmatrix} \sum_{i=1}^{n_P} \varepsilon_i \\ \sum_{i=1}^{n_P} \xi_i \varepsilon_i \\ \vdots \\ \sum_{i=1}^{n_P} \xi_i^k \varepsilon_i \end{Bmatrix} \tag{34}$$

where n_P is the number of points to be regressed, and ε_i is the discrete strain data obtain during the experimental test from sensors. These set of equations can be represented in a general form of $\mathbf{H} = \boldsymbol{\alpha}\mathbf{Q}$ and the coefficients α_k can be determined as:

$$\alpha_k = \frac{\det(\mathbf{H}_i)}{\det(\mathbf{H})} \tag{35}$$

where the $\mathbf{H}_i$ is a new matrix with the i-th column replaced by the column vector $\mathbf{Q}$. An example of $\mathbf{H}_0$ matrix computation can be found in [56]. Solving these equations for different polynomial order, the best curve fit for the discrete experimental strain measurements can be obtained and accordingly the results of pre-extrapolated strains can be employed in iFEM-iQS4 analysis.

3. Numerical and Experimental Examples

In this section, the ability of the iFEM method to reconstruct the geometrically non-linear deformation of thin laminated plates and shell structures is thoroughly investigated numerically and experimentally. The numerical problems involve flat and curved laminated panels subjected to increasing compressive load and exhibiting geometrically non-linear buckling and bending deformations. In the experimental case, a rectangular thin laminated plate is subjected to a line load that leads to deformation with a large deflection in the center of the plate. It should be noted that these case studies are carefully selected to demonstrate the inherent geometric application of

14

the iFEM-iQS4 element for flat and curved thin laminated composite panels. As mentioned earlier, strain values have a critical role in iFEM shape sensing methodology. These required strain data are obtained for the numerical problems by performing non-linear FEM analysis utilizing ANSYS-APDL software [64]. However, these strain values are collected for the experimental case by using a network of strain gauges on the surface of the plate. To improve the accuracy of iFEM analyses with discrete in-situ strain data, a polynomial extrapolation strategy is used to smooth the discrete in-situ strain data. Finally, all the numerical and experimental results are verified using high-fidelity FEM analyses.

3.1 Post-buckling Analysis of a Flat Laminate: First Numerical Case Study

A carbon fiber reinforced polymer (CFRP) laminate with a square shape of 1 [m^2] area is considered as shown in Fig. 4. The stacking order of the laminate is [$\pm$ 30]$_{3s}$, with a total of 12 layers symmetric about the midplane. Each layer has a thickness of 0.3 [mm], resulting in a total laminate thickness of 3.6 [mm]. The right edge of the plate is rigid, and a concentrated axial load of 60 [kN] is applied across this rigid end, thereby resulting in a uniform displacement in the negative x-direction, as depicted in Fig. 4. Since the load is applied so slowly that there are no dynamic effects within the structure, which is called quasistatic, the non-linear nature of the problem requires that the load be increased gradually. The initial load of 600 [N] is applied and then ramped to 60 [kN] with 17 incremental steps. Nonlinear analyses are performed using FEM software (i.e., ANSYS APDL). This software uses Newton-Raphson convergence criteria for nonlinear problems. The maximum number of equilibrium iterations is set to 1000 in ANSYS for each load increment to ensure a correct convergence and load-equilibrium analysis.

The left edge of the laminated plate is fully clamped. However, only the transverse displacement w and bending rotation about the y-axis θ_y are considered constrained for both top and bottom edges of the plate, as shown in Fig. 4. The mechanical properties of the CFRP material are listed in Table 1. This post-buckling analysis aims to evaluate the ability of the iFEM analyses to track the variations of the translational and rotational displacement at points A, B, and C as the load increases (the exact positions of points A, B, and C are depicted in Fig. 4). For this purpose, a non-linear FEM analysis is performed to simulate the required strain data as input to the iFEM analysis.

15

Table 1. Mechanical properties of the CFRP material

Lamina material	Young's modulus [GPa]	Poisson's ratio	Shear modulus [GPa]
Carbon-epoxy unidirectional composite	$E_1^{(k)} = 157.9$	$\nu_{12}^{(k)} = \nu_{13}^{(k)} = 0.32$	$G_{12}^{(k)} = G_{13}^{(k)} = 5.93$
	$E_2^{(k)} = E_3^{(k)} = 9.584$	$\nu_{23}^{(k)} = 0.49$	$G_{23}^{(k)} = 3.227$

The entire area of the plate is discretized into 100 sub-areas, as shown in Fig. 5. Three types of sensor placement models, namely 'Model I', 'Model II', and 'Model III' are used to perform the iFEM analyses at the same mesh resolution. In the arrangement of sensors for Model I, all inverse elements contain two strain measurement sets at the center of the element at two different interlaminar positions. These positions are chosen preferably through the thickness of the laminate (as mentioned in Section 2) with a total number of $2 \times 100 = 200$ strain rosettes. The sensor placement strategy of Model II uses $2 \times 40 = 80$ strain rosettes placed in the center of 40 elements. In the last sensor configuration (Model III), the total number of strain rosettes is reduced to $2 \times 16 = 32$ sensors, as shown in Fig. 5.

The weighting coefficients for elements owning sensors at the middle are assigned as $w_e = w_\kappa = 1$ and $w_\gamma = 10^{-7}$. However, for elements without sensors, these constants are set to $w_e = w_\kappa = w_\gamma = 10^{-4}$. It is worth noting that although thin plates undergo large deformations, but the strain values remain small, i.e., 1 to 10 micro strains. Therefore, when performing iFEM analyses, it is not practical to update the in-plane geometry and sensor positions with respect to each time step. However, the out-of-plane geometry (i.e., deflection) of the plate may need to be updated at each loading step. Since there is no significant deflection between each time step, a linear iFEM analysis is preferred in the first numerical case compared to incremental linear iFEM analysis.
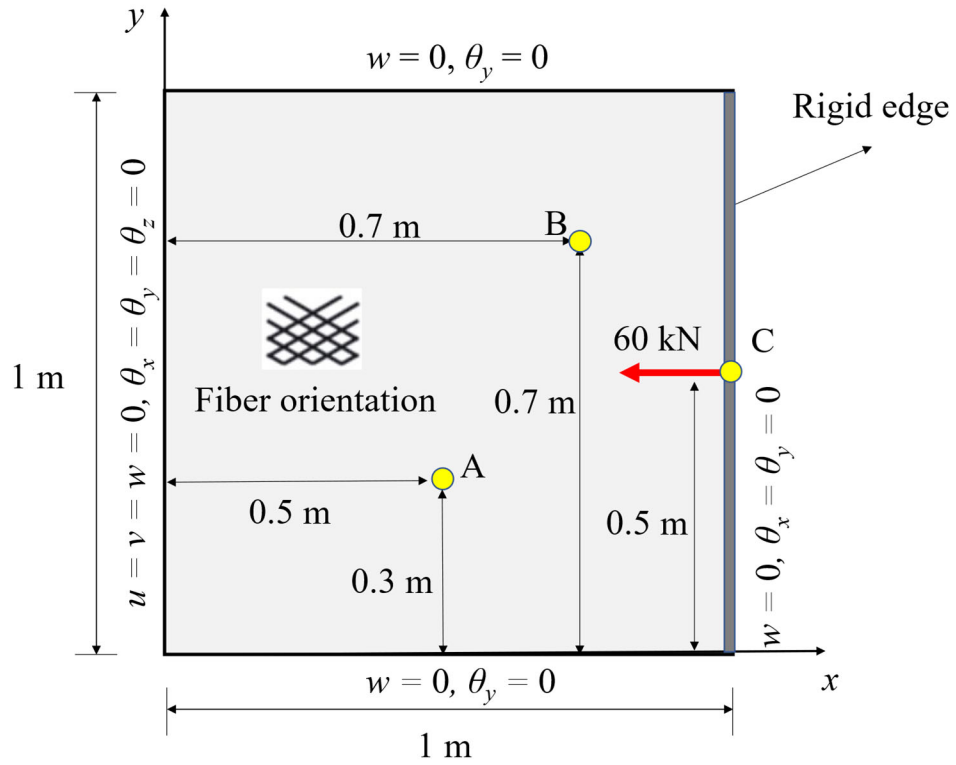
Fig. 4. Dimensions, fiber orientation, and boundary conditions of the laminated plate.
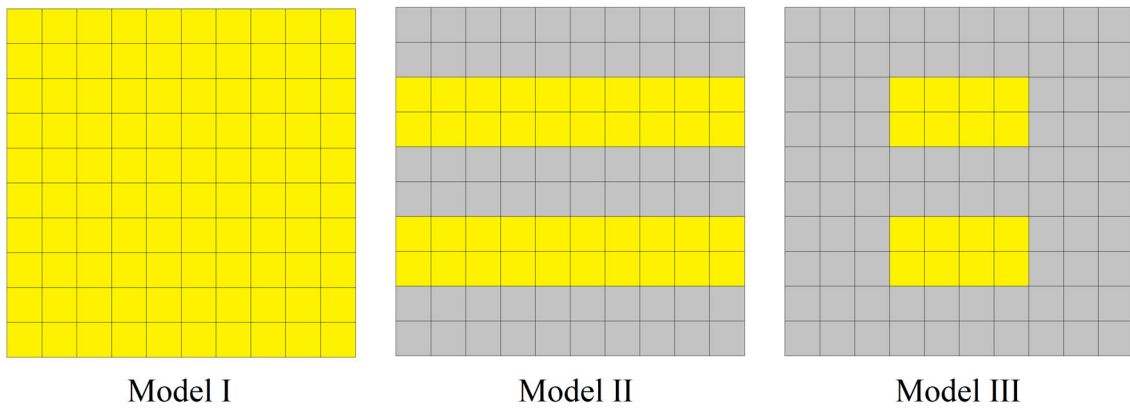
Fig. 5. Different sensor placement models of the plate.

Model I

Model II
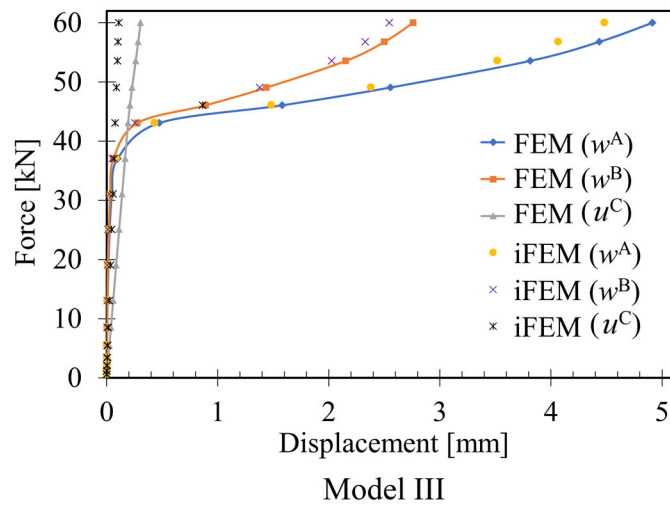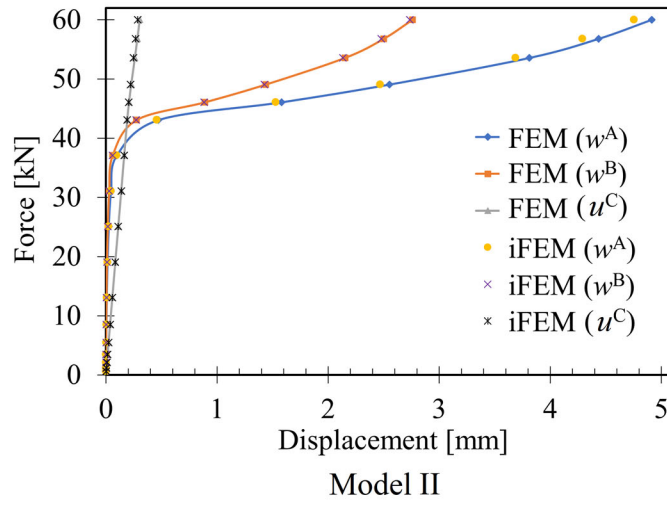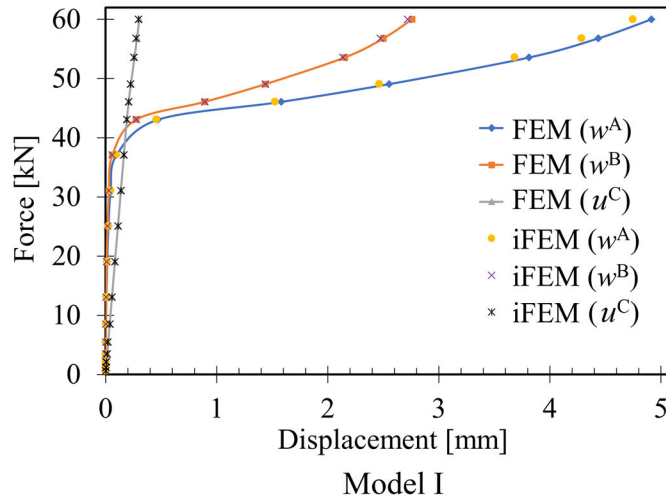
Model III
Fig. 6. Variation of transverse and axial displacement components at points A, B, and C.
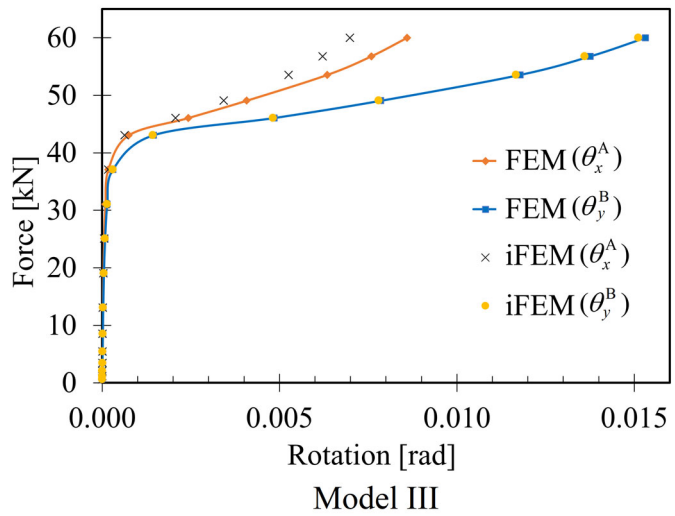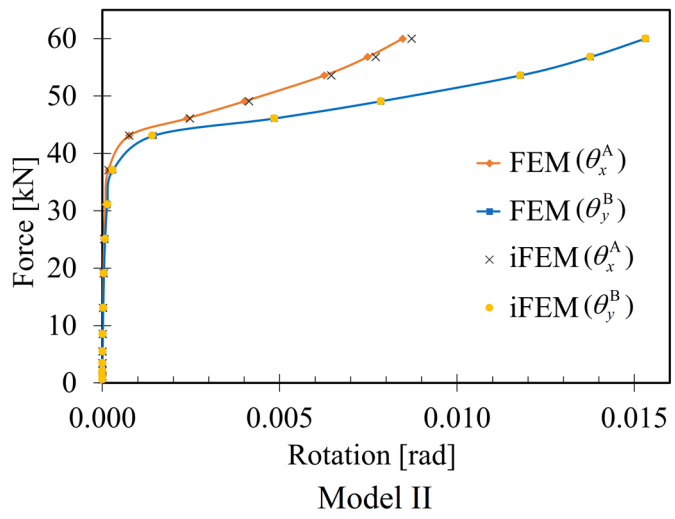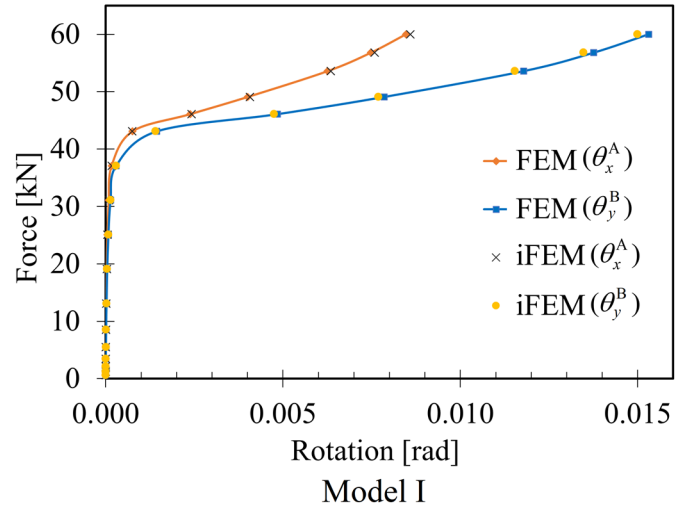
Fig. 7. Variation of rotational displacement components at points A, and B.

Fig. 6 shows the change in z-displacements w for points A and B, and the absolute value of x-displacement u at point C under incremental loading obtained by FEM and iFEM analysis using three types of sensor configuration. Moreover, the rotation variation about the x-axis θ_x for point A and the y-axis θ_y for point B is illustrated in Fig. 7. The force-displacement diagrams (Fig. 6, 7) exhibit that points A and B of the plate experience linearly transverse and rotational displacement almost up to 35 [kN] load level. After that, as the load increases, the plate experiences geometrically non-linear deformations up to 60 [kN]. However, point C experiences bilinear axial deformation throughout the loading history, as shown in Fig.6. It can be observed from Figs. 6-7 that the iFEM can accurately capture the bilinear and non-linear behavior of the plate using Model I and Model II. However, regarding Model III, the iFEM results are slightly deviating from FEM results due to a smaller number of sensors, but it can still forecast the trend of FEM results.

The contour plots of obtained transverse and rotational displacements are compared between FEM and iFEM analyses with different sensor deployments are shown in Figs. 8-10. These figures show that the last time-step contour plots of transverse and rotational displacement of iFEM analyses are compared with the reference FEM solution. It can be seen from these figures that the iFEM results are quite similar to each other and almost indistinguishable from the FEM result. These contour results confirm the superior ability of the iFEM-iQS4 element to reconstruct post-buckling analyses of thin laminates.

To compare the quantitative results related to Figs. 8-10, a percent differences calculation is performed between maximum values of FEM and the iFEM analyses. In this regard, the percent differences between the reference solution and the iFEM analyses using sensor positions of Model I to III for the maximum transverse displacement are about 0.0%, 0.15%, and 5.4% in the given order. However, the same comparison for the maximum rotation about the x-axis between FEM and the iFEM analyses are 0.0%, 0.03%, and 1.1%, respectively. Finally, the comparison between the FEM and iFEM analyses for the maximum rotation about the y-axis are 0.45%, 2.5%, and 3%, respectively. This quantitative evaluation proves that iFEM is accurate enough to predict the maximum values of the translation and rotation field with only a small margin of error, even when only a few discrete sensor data are used.
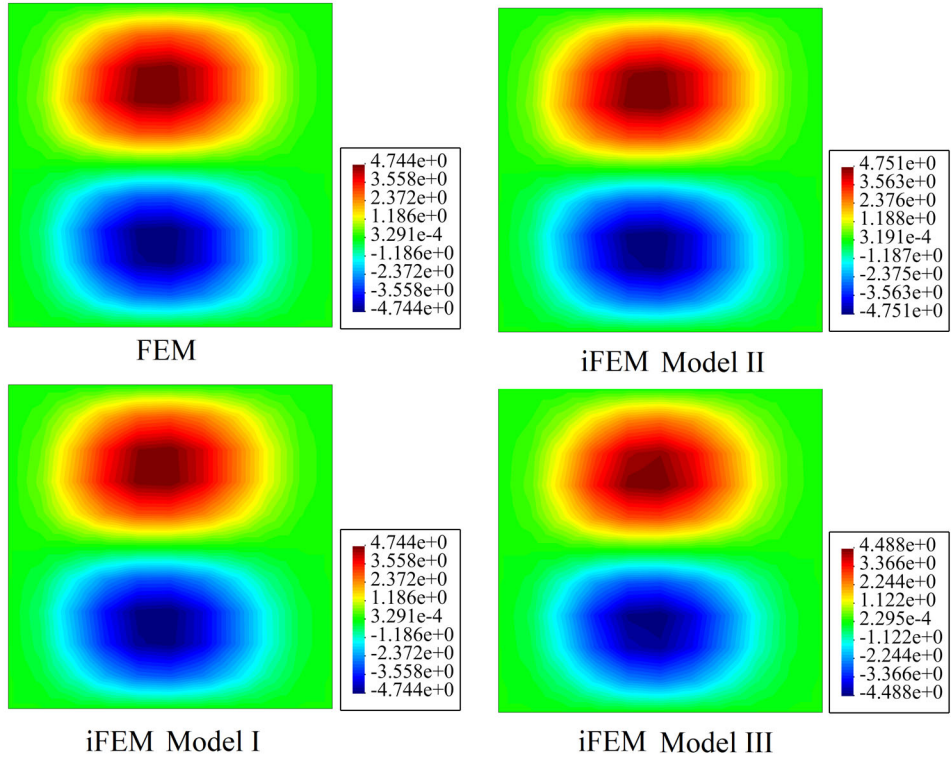
Fig. 8. Contours of transverse displacement w [mm] between FEM and iFEM analyses.
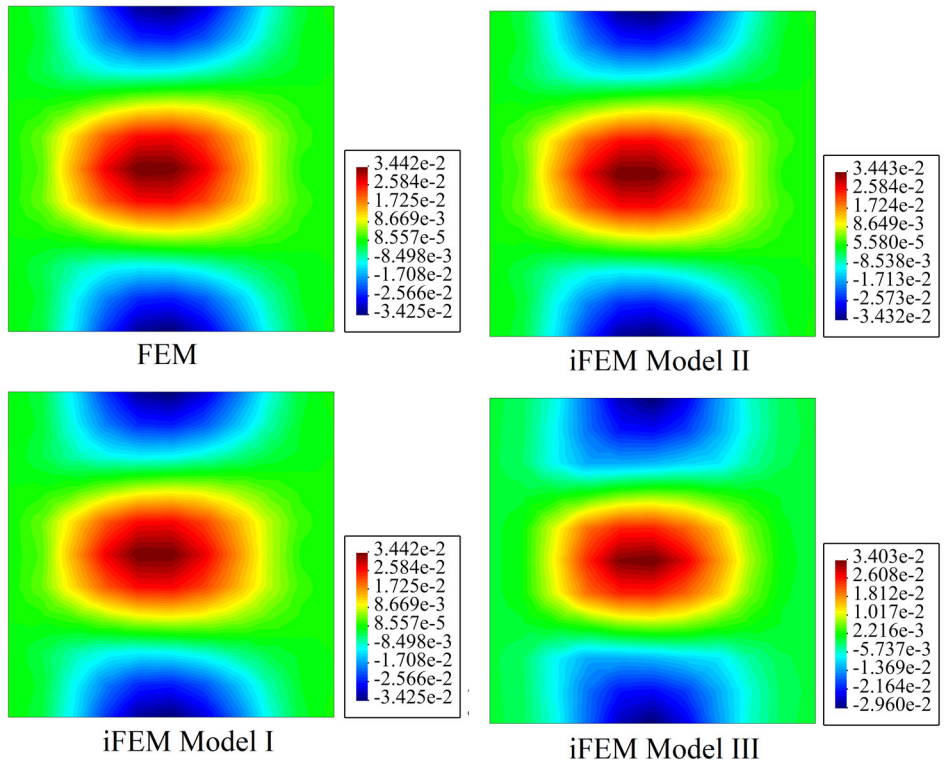
Fig. 9. Contours of rotation [rad] around x-axis between FEM and iFEM analyses.
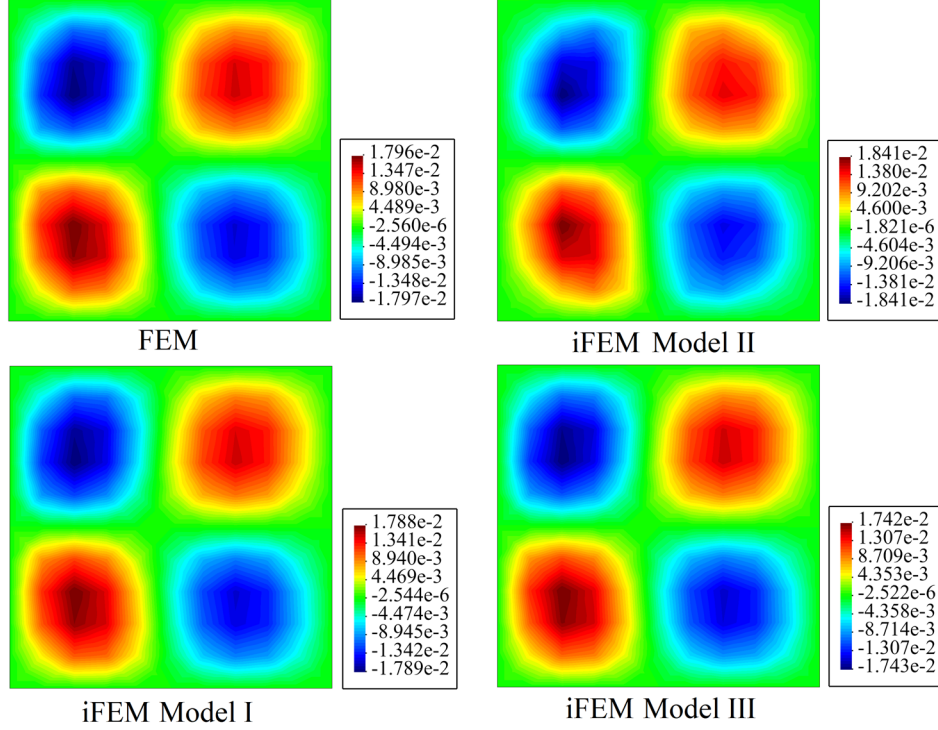
Fig. 10. Contours of rotation [rad] around *y*-axis between FEM and iFEM analyses.

3.2 Large Deflection of a Clamped Laminated Cylindrical Panel: Second Numerical Case Study

A deep cylindrical CFRP laminated plate under a point load with a stacking order of $(0/90/0/90)_s$ is evaluated by iFEM analyses. The geometry and boundary conditions are similar to a benchmark problem performed in some preliminary studies [65] with the following data: $R = 500$ [mm], $L = 450$ [mm], $\beta = 30^\circ$, $h = 4$ [mm] (refer to Fig. 11). The plate is subjected to gradually increasing concentrated loads of a maximum of 4 [kN] to achieve geometrically non-linear deflection. Like the previous example, three sensor positions are used to provide the required strain values for the iFEM formulation. Herein, the whole curved domain is divided into 144 sub-elements. For the first type of sensor distribution, indicated by the legend 'Model I,' all elements are instrumented using $2 \times 144 = 288$ strain sensors. The second model of sensor deployment is labelled as 'Model II', and the number of sensors is reduced to half ($2 \times 72 = 144$). However, for the third model of sensor distribution, 'Model III', the number of rosettes is reduced to one-sixth ($2 \times 24 = 48$) as shown in Fig. 12. The weighting constants for elements with sensors are set as $w_e = w_\kappa = 1$, $w_\gamma = 10^{-6}$. However, for elements without sensors, they are assigned as $w_e = w_\kappa = w_\gamma = 10^{-3}$.

22
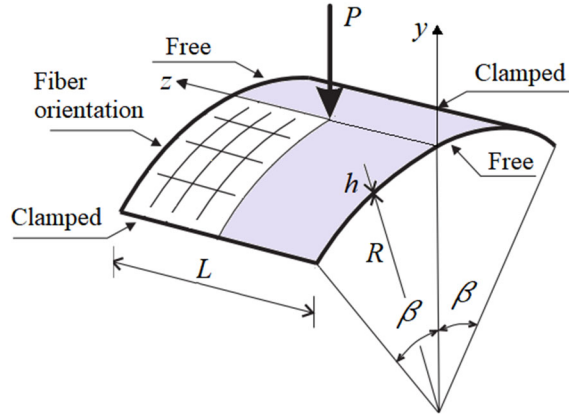
Fig. 11. Clamped laminated cylindrical panel under point load.

Model I   Model II   Model III
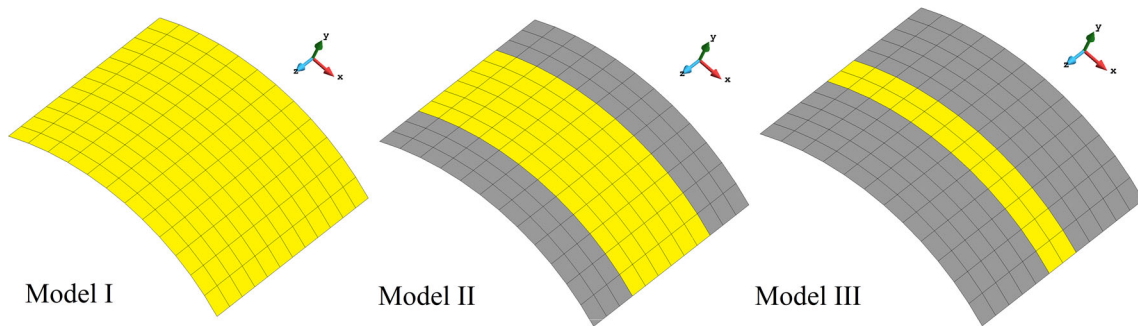
Fig. 12. Different types of sensor placement for cylindrical panel.

The capabilities of iFEM analyses in terms of shape sensing of curved laminates under point loads are evaluated. The central point of the laminate is subjected to a gradually increasing load of a maximum of 4 [kN]. The load is applied to the structure in ten increasing steps with equal intervals of 400 [N], as shown in Fig. 13. In this way, the central point of the plate is deflected as a function of incremental forces. Since the incremental strain values associated with the alternating time-steps are large enough to affect the deflection results of the iFEM analyses, the incremental linear iFEM formulation is applied at each loading step to reconstruct the current deformed shape. Then, the geometry is updated, and the iFEM analyses are performed based on the incremental strain data utilizing three types of sensor configurations (i.e., Models I to III). Fig. 13 obviously shows that the deflection predicted by the linear incremental iFEM approach agrees quite well with the FEM solution when the first sensor model is used. It is also clear that as the number of strain gauges decreases, there is a discrepancy between the linear incremental iFEM and FEM results. However, these error margins are negligibly small, indicating that the incremental linear iFEM approach can capture well the geometrically non-linear deflection of a thin laminated shell structure. The linear iFEM results are calculated and compared with the FEM solution and are

23

exhibited in Fig. 13. In the current case study, it can be observed that, unlike the previous numerical example, linear iFEM analyses cannot be a substitute for the shape sensing of curved laminates.
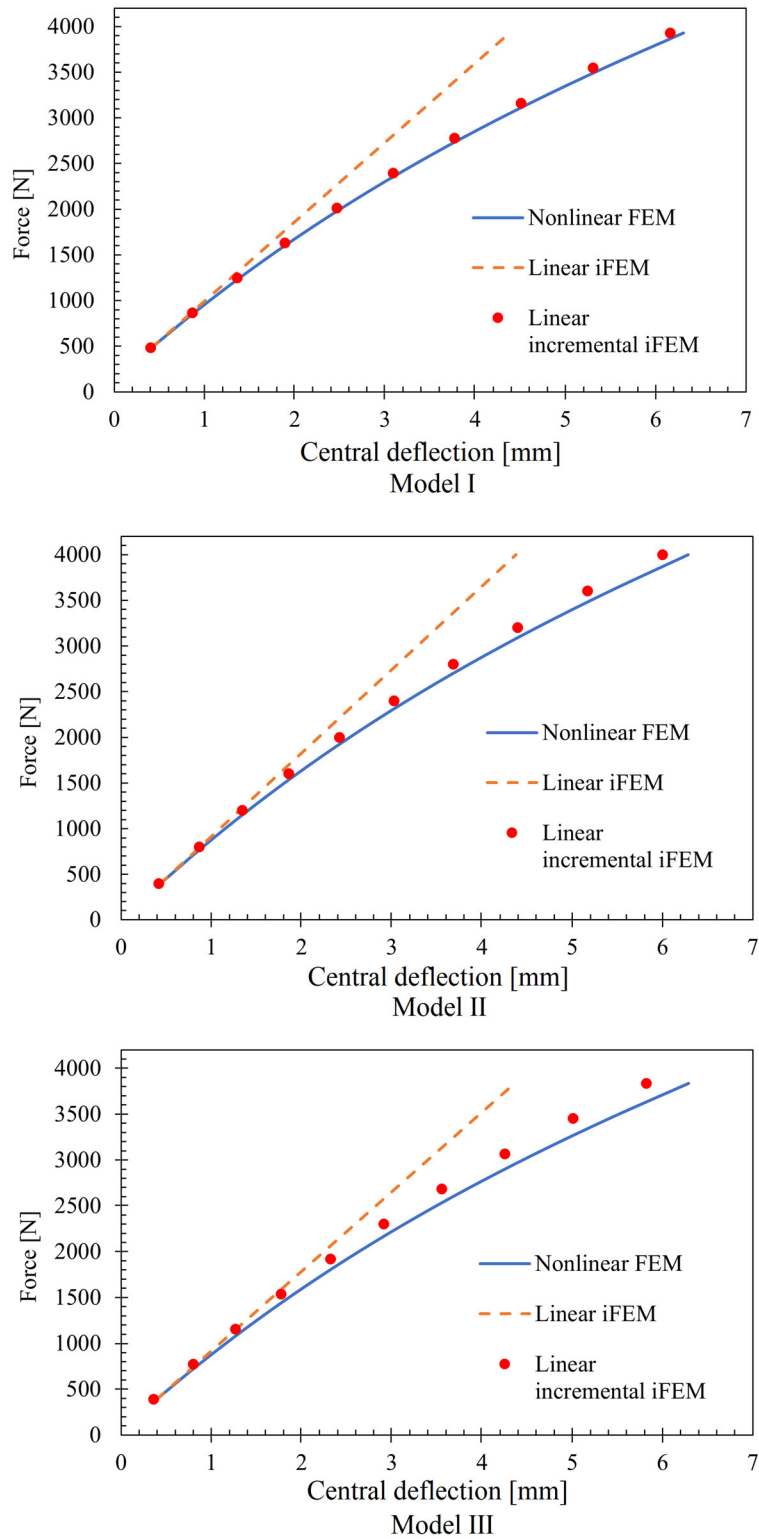
Fig. 13. Central deflection of the cylindrical laminate using three types of sensor placement.
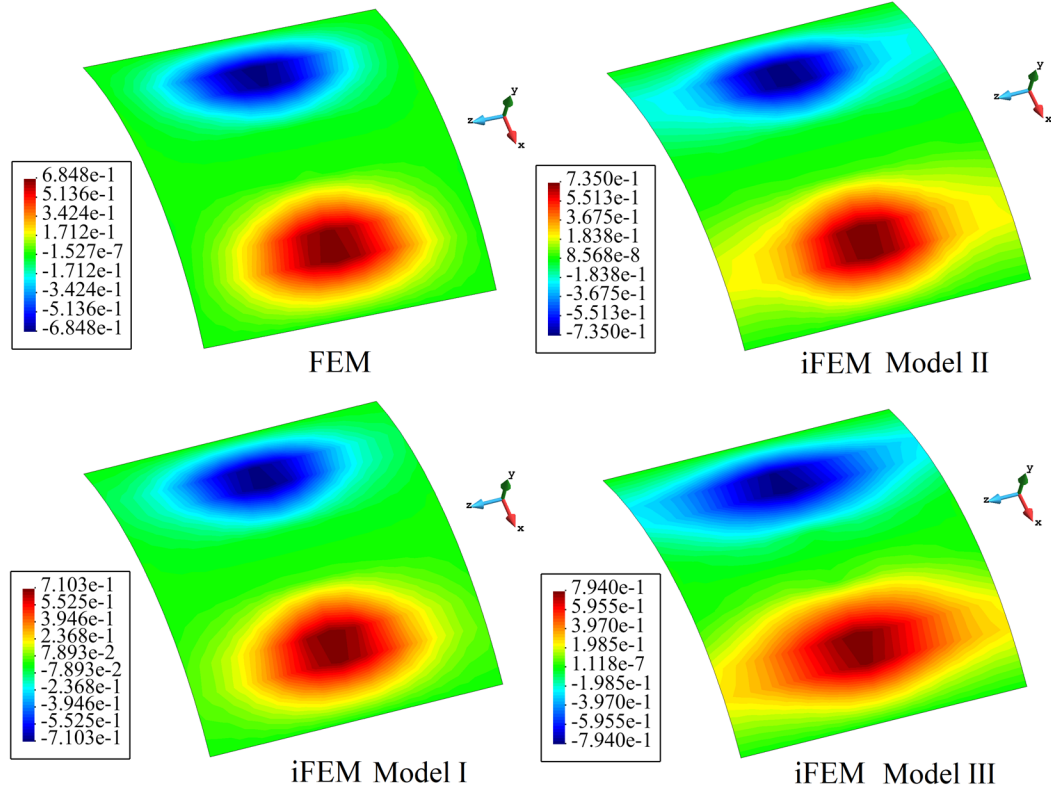
Fig. 14. Contours of *x*-displacement [mm] component obtained by iFEM and FEM analyses.

Additionally, the ability of the incremental iFEM approach to reconstruct the axial and rotational displacements of the last time-step using the Model I, Model II, and Model III sensor configurations are illustrated in Figs. 14-16. These axial and rotational displacement contours show that the iFEM analysis with the sensor distribution of Model I reconstructs quite similar contours to the reference FEM solution. Moreover, the obtained contours of the iFEM analyses with the Models II and III sensor configuration are less accurate but still comparable to FEM solutions. It should be noted that although the use of a smaller number of sensors leads to a minor contour inconsistency compared to the reference solution, it predicts the precise location of the occurrence of the maximum displacement, which fulfills the most crucial requirement of a reliable shape sensing system.
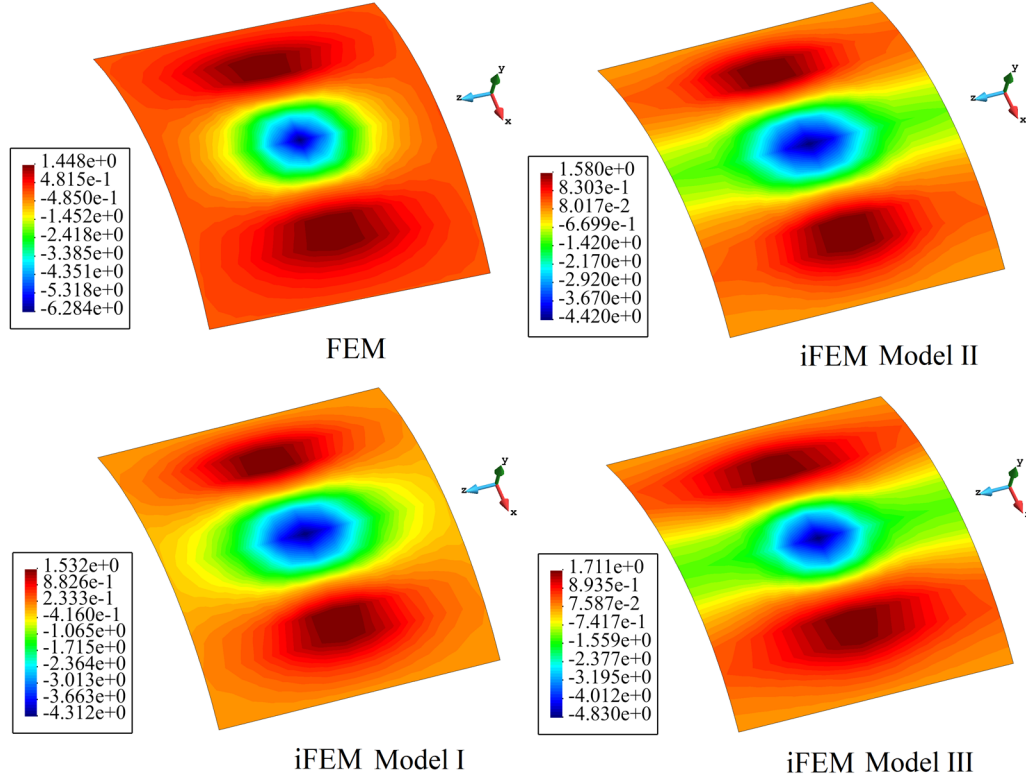
Fig. 15. Contours of *y*-displacement [mm] component obtained by iFEM and FEM analyses.

Quantitatively speaking, the percent differences for the maximum x and y displacements between the FEM reference and the iFEM analyses are calculated as (3.7%, 7.3%, 16%) and (5.8%, 9.1%, 18%), respectively, for the Models (I, II, III). However, when a similar comparison is made between FEM and iFEM analyses for the case of rotation θ_z (around global z-axis), these margins of error are reduced to 0.04%, 0.9%, and 0.91% in the given order. These values for the percent difference show the superior performance of the iFEM approach at a higher sensor density, especially at the maximum rotational displacement. Although the values for the percent difference increase at lower sensor densities, these error percentages are not significant enough to affect the reconstruction performance of the iFEM method. Overall, based on the obtained quantitative and qualitative results, it can be declared that the iFEM-iQS4 element is efficient enough to reconstruct the non-linear deformations as well as the axial and rotational contours with only a few sensors. These two numerical investigations clearly illustrate that using iFEM analyses for shape sensing of thin laminated plates and shells leads to reliable and cost-effective results.
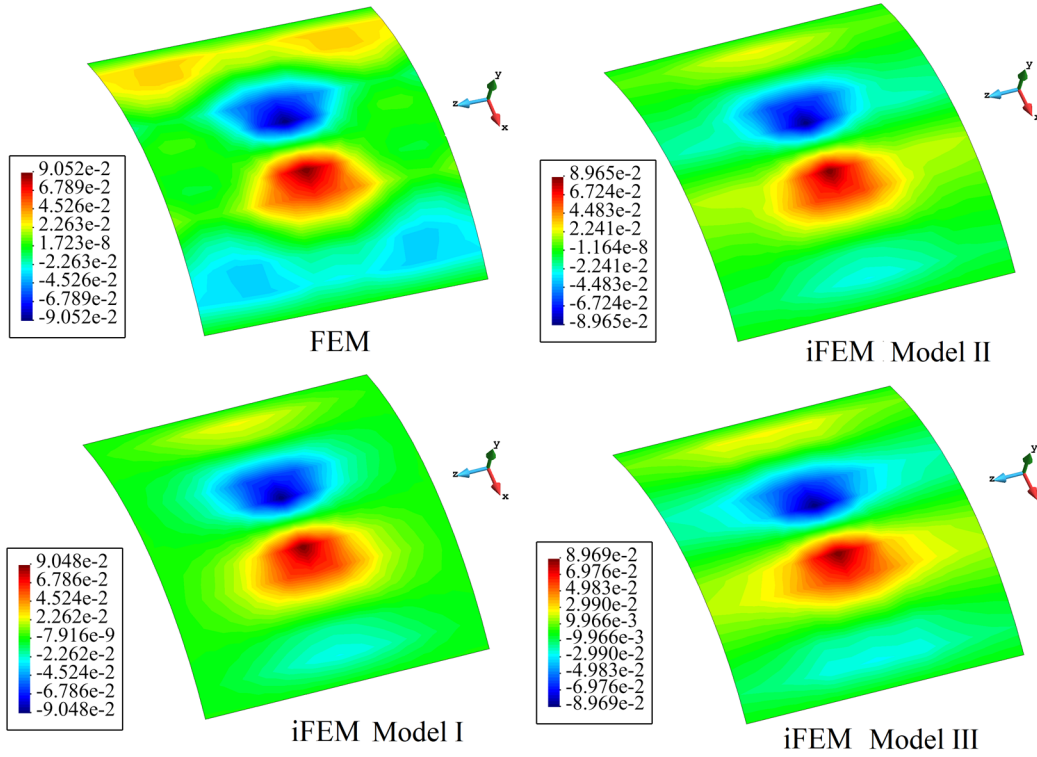
Fig. 16. Contours of rotation [rad] around *z*-axis obtained by iFEM and FEM analyses.

3.3 Large Deflection Sensing of a Clamped Laminated Flat Panel: Experimental Case Study

3.3.1 Laminate manufacturing and testing

E-glass fiberglass woven roving fabric with an areal weight of 300 g/m^2 and Biresin CR120 resin and CH120 hardener were procured from Metyx-Turkey and Sika for fabrication, respectively. The vacuum-assisted resin infusion process is used to fabricate the composite sheet with a uniform thickness of almost 0.83 [mm]. For the resin infusion, a flat stainless-steel surface of the table was prepared by applying coats of sealant and release films. Four layers of fibers were placed on the prepared surface and covered with a peel ply and then flow-mesh, which helps prevent the air entrapment and assists the uniform resin flow. A vacuum bag was sealed with the help of sealant tape, and then a debulking process was carried out for 30 minutes. Resin and hardener were mixed in a ratio of 100:30 wt% and then degassed for 20 minutes to remove entrapped air. After degassing, epoxy was injected into the system, and a temperature of 120ºC was applied through Wittmann Tempro plus D-18 for 24 hours. The samples from the composite

27

plate were machined by a Kuka KR16 Ultra-F-robot water jet to characterize the material properties.
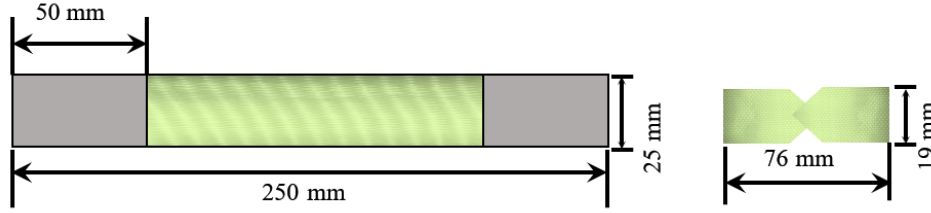
Fig. 17. The schematics of tensile and shear test specimens.

Table 2. Mechanical properties of the Glass-Epoxy material

Lamina material	Young's modulus [GPa]	Poisson's ratio	Shear modulus [GPa]
Glass-epoxy twill composite	$E_1^{(k)} = E_2^{(k)} = 24$ $E_3^{(k)} = 7.1$	$v_{12}^{(k)} = v_{13}^{(k)} = v_{23}^{(k)} = 0.14$	$G_{12}^{(k)} = G_{13}^{(k)} = G_{23}^{(k)} = 3.1$

Tensile test was performed according to ASTM D-3039 standard to determine the elastic modulus and Poisson's ratio, whereas Iosipescu shear test was performed as per ASTM D5379 to measure the shear modulus. For the tensile test, six specimens with a size of 250×25 [mm^2] were cut and tabbed with 50 [mm] aluminum, while for the shear test, five specimens with a size of 76×19 [mm^2] were tested. Both shear and tensile tests were performed with the help of the Instron universal testing machine (UTM) 5982, which is equipped with a 100 [kN] load cell. Fig. 17 depicts the schematic of tensile and V-notch shear test specimens. The obtained mechanical properties of the glass-epoxy material are listed in Table 2. It is noteworthy that a bending test cannot determine the out-of-plane material properties because the plate is not thick enough. Therefore, these material properties are approximated and calibrated using the FEM analysis.

3.3.2 Large deformation test setup

For the large deformation test setup, sixteen Type I C2A-06 125ww-350 strain gauges with quarter bridges are used to measure the strain. These strain gauges have a grid resistance of $350 \pm 0.6\%$ [Ohms] and are stacked as 0º-45 º-90 º rosette, recommended for steep strain gradient and limited gaging areas. These strain gauges are attached to the bottom of the 1200×300 [mm^2] composite laminate. The laminate is fixed in a metal fixture, and a compression line load is applied along the length of the laminate (refer to Fig. 19). The geometry, boundary conditions, and sensor

positions of the clamped flat plate are shown in Fig. 18. The whole area of the plate is discretized into several elements. Some of these elements have sensors at their centers marked with yellow color as seen in Fig. 18. The exact location of these sensors is shown in Table 3.

Table 3. Coordinates of sensors on experimental laminated plate

Sensor	x [mm]	y [mm]	Sensor	x [mm]	y [mm]
1	1100	75	9	1100	225
2	900	125	10	900	275
3	700	75	11	700	225
4	900	25	12	900	175
5	500	75	13	500	225
6	300	125	14	300	275
7	100	75	15	100	225
8	300	25	16	300	175
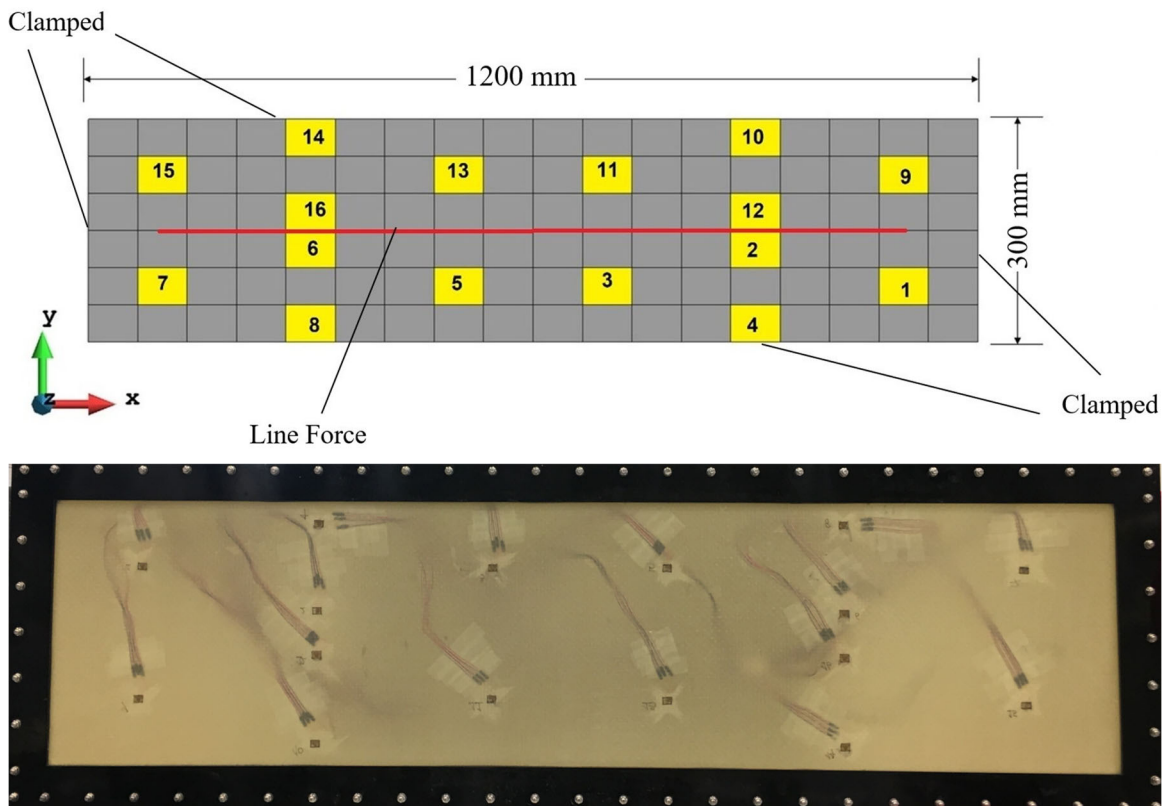
Experimental Sensor Placement on the Composite Plate

Fig. 18. The geometry, boundary conditions and sensor positions of the flat plate under line load.

Strain data is acquired using the NI PXIe-1075 chassis via the NI 6363 strain card, using the NI signal express software to record the continuous data. To achieve a homogeneous distribution of strains, a preload of 100 [N] is applied to the surface of the plate via a steel bar. At a preload of 100 [N], the strain gauges are calibrated to use the zero value as a reference. A continuous ramp load of 100 [N] to 750 [N] with a hold time of 10 seconds between each ramp is applied to the plate within an interval of 250 seconds, as shown in Fig. 20. Strain data are post-processed using NI- DIAdem 2021 software, where strain data for each 10-second hold step (13 in total) from each strain gauge are averaged and then used for iFEM calculations. As shown in Fig. 18, the arrangement of the sensors and the applied boundary condition are symmetrical, which also results in symmetrical strain data. Therefore, one set of strain gauges (1 to 4) can represent the strain distribution across the whole laminate. Fig. 21 shows the non-linear variation of axial strains of these sensors (1 to 4) over the time-steps.
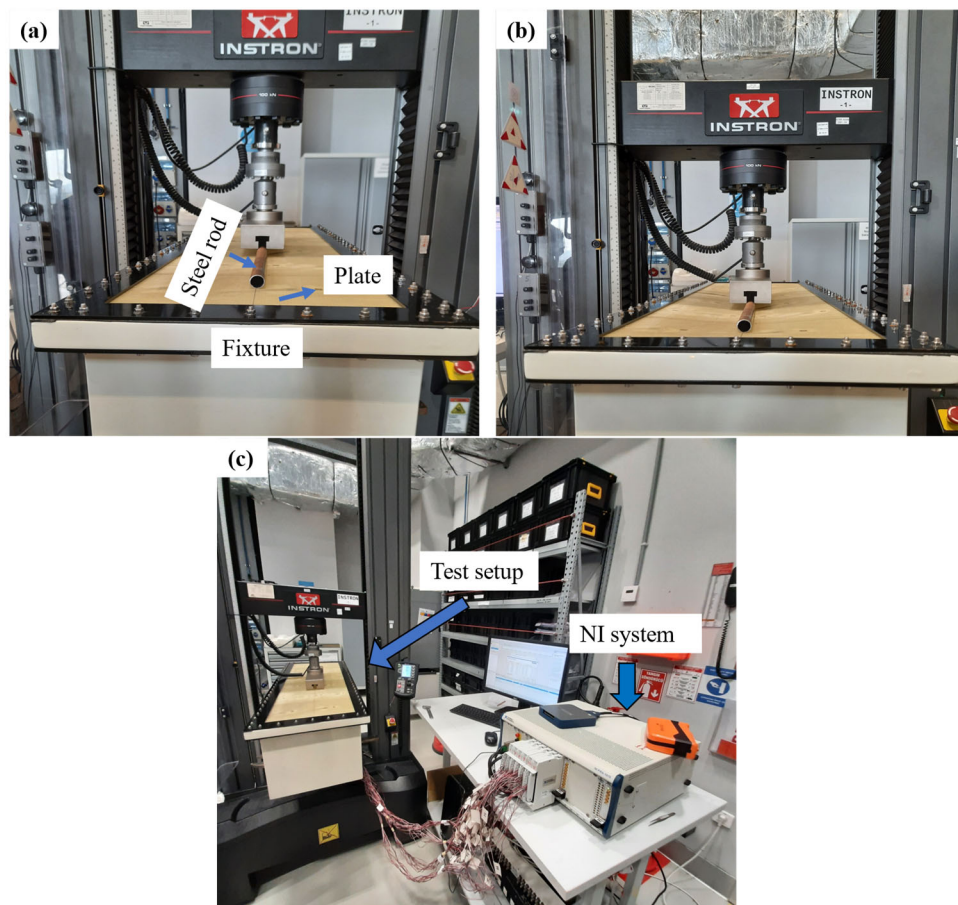
Fig. 19. Test setup a) before loading, b) after loading, c) data acquisition system.
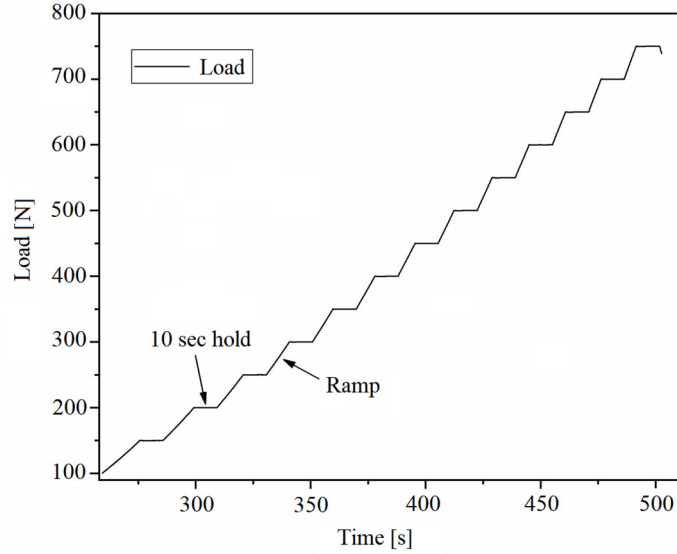
Fig. 20. Time-loading history.
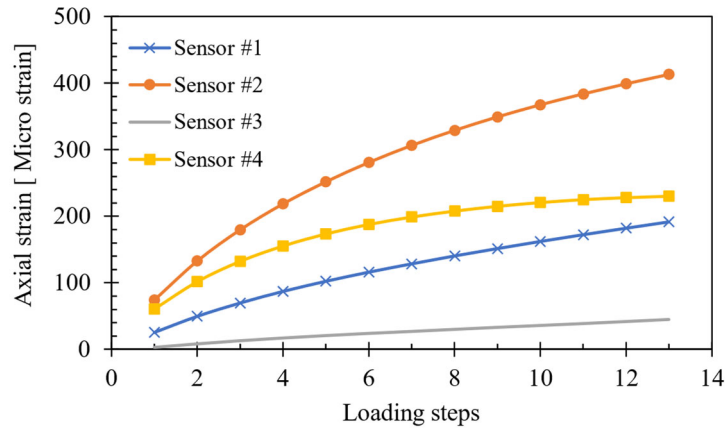
Fig. 21. The variation of axial strains of sensors number 1 to 4 over the time steps.

3.3.3 iFEM-based Shape Sensing

This section presents real-time shape sensing for the clamped laminated plate by performing iFEM analyses. As described in the previous sections, a prior smoothing analysis is performed over the obtained experimental strain data. For this purpose, a moderately fine resolution of the iFEM discretization is used with discrete strain data obtained through strain gauges, as shown in Fig. 22(a). After that, the missing strain values of the empty elements are predicted by performing a strain pre-extrapolation technique to fit a fourth-order polynomial curve through discrete strain values aligned along the *x*-axis (Fig. 22b). Thus, the number of available strain data is increased

31

from sixteen to forty-four, and this extensive strain data is used in the iFEM formulation. The iFEM analyses are then performed for all incremental loading steps to reconstruct the non-linear large deflection of the entire laminate. The weighting values for the elements accommodated with sensors are set as $w_e = w_\kappa = 1$ and $w_\gamma = 10^{-6}$. However, these constants are assigned as $w_e = w_\kappa = w_\gamma = 10^{-5}$ for elements without sensors (strain-less elements). Finally, a high-fidelity FEM analysis with 14701 nodes and 88206 DOFs is performed to serve as a reference solution to compare with the iFEM results (Fig. 22c).
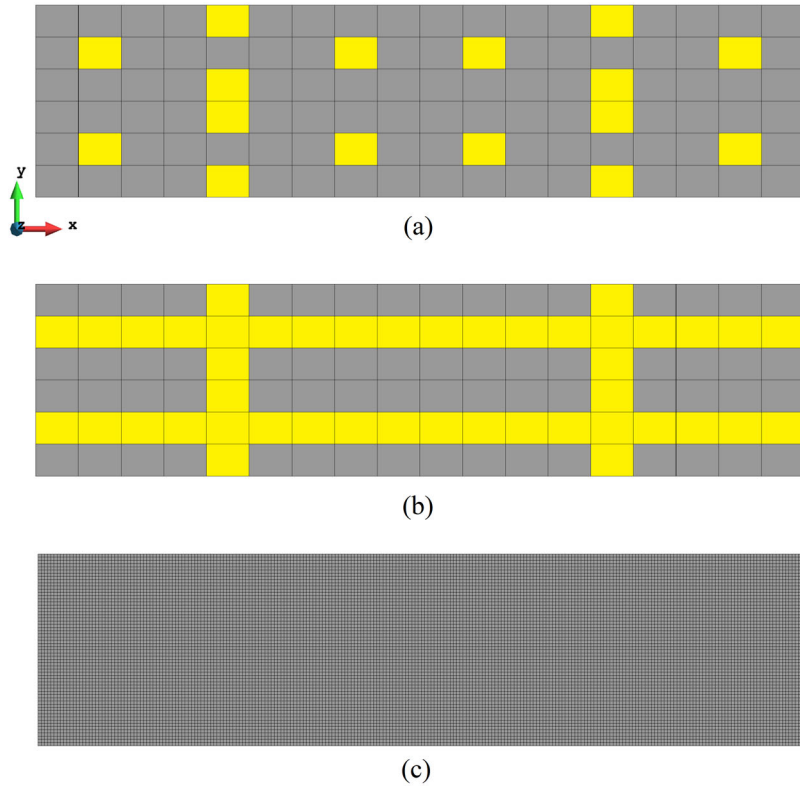
Fig. 22. Mesh resolution and iQS4 elements with strain measurement sets at the center for a) iFEM analysis using discrete sensors, b) iFEM analyses using polynomial smoothing approach, and c) FEM model.

The central deflection (maximum displacement) of the laminate for all loading levels obtained by experiment, FEM, iFEM using discrete strain data, and iFEM coupled with the pre-extrapolation technique are shown in Fig. 23. This figure shows that the iFEM (pre-extrapolated strain data), experimental results and FEM analyses have a higher degree of agreement compared to iFEM (discrete strain data), thereby proving the advantage of the strain extrapolation before

32

running an iFEM analysis. In other words, the use of polynomial smoothing analyses for iFEM analysis results in almost identical nonlinear deflection predictions to the experimental deflections and reference FEM solutions, whereas iFEM analysis with discrete strains underestimates the maximum deflections as shown in Fig. 23. This behaviour is even more apparent at the higher loading levels (after load step of 6). For smaller loads (before load step 6), both iFEM approaches produce more erroneous deformations due to the fully clamped constrained boundary condition of the plate and unavailability of adequate sensors near the clamped edges as can be observed from Figs. 22a-b. This means that in the lower loading stages, the strains dominate at the edges of the laminates whereas, at higher load levels, these strain magnitudes become smaller as compared to the strains at the centre of the plate, thereby allowing a better deformation reconstruction after load step of 6. In sum, since the edge lines of the plate do not have a sufficient number of sensors to detect these experimental strains, the iFEM-reconstructed displacements at low loading levels become less accurate than that of the higher loading stages.
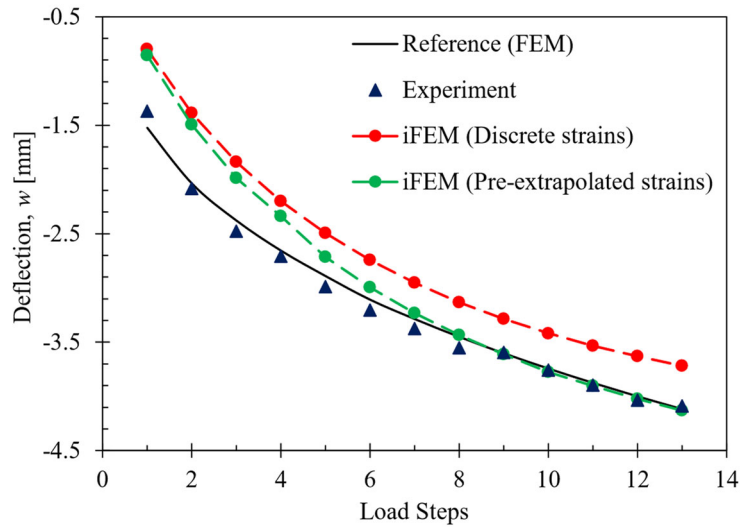
Fig. 23. Central deflection of the plate obtained from experiment, FEM analysis, and iFEM analysis.

Figs. 24-26 illustrate full-field deflection of the plate obtained with iFEM using discrete and pre-extrapolated strains and FEM analyses for three arbitrarily selected time loading levels (i.e., steps 3, 8, and 13). As can be seen in these figures, the total displacement contours obtained using iFEM in conjunction with a polynomial smoothing approach are comparable to the reference FEM, which also confirms the high performance of the iFEM method for full-field reconstruction in real-time. However, the iFEM analyses with discrete strains show lower accuracy in reconstructing the

33

full-field displacement contours. In terms of numbers, the maximum values of the total displacement between FEM and the iFEM analyses using the strain pre-extrapolated technique are 12%, 0.9%, and 0.3% for steps 3, 8, and 13, respectively. However, the percentage errors between FEM and the iFEM analyses using discrete strain data are 21%, 7.5%, and 7% in the given order, confirming the higher accuracy and efficiency of the iFEM analyses using the pre-extrapolated strain data.
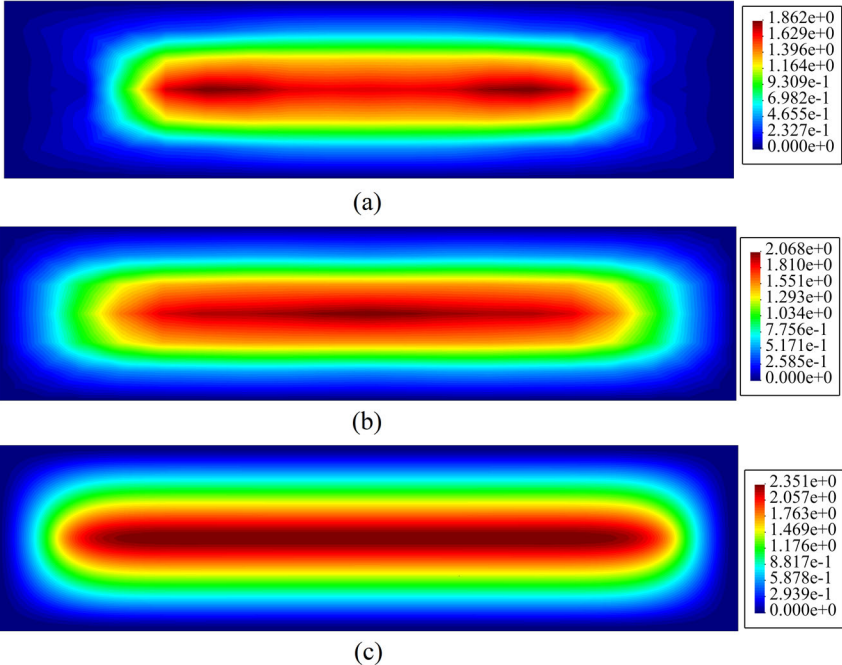
Fig. 24. Total displacement contours at time-step 3 obtained by (a) iFEM analysis using discrete sensors, (b) iFEM analysis using polynomial smoothing approach, and (c) FEM analysis.
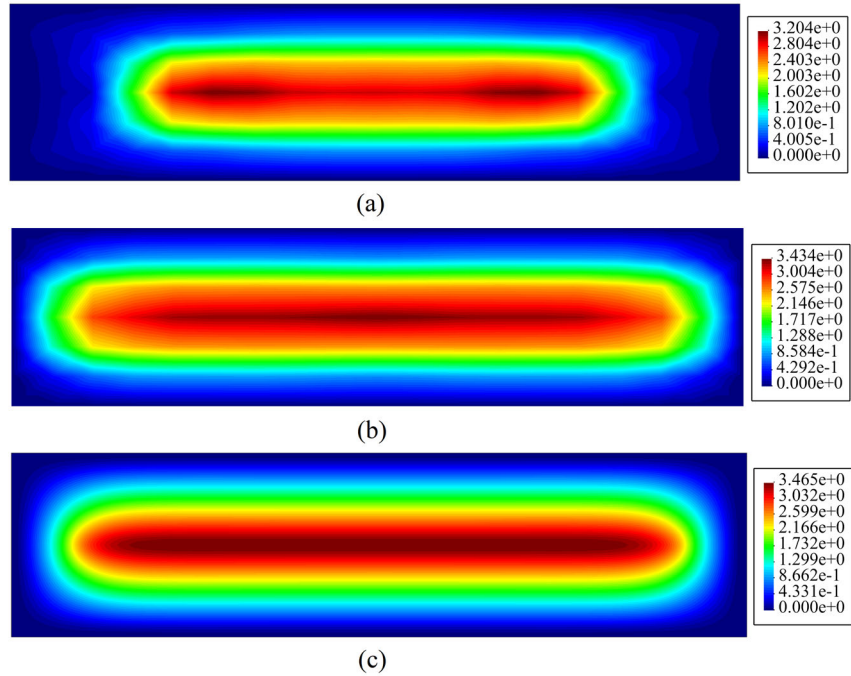
Fig. 25. Total displacement contours at time-step 8 obtained by (a) iFEM analysis using discrete sensors, (b) iFEM analysis using polynomial smoothing approach, and (c) FEM analysis.
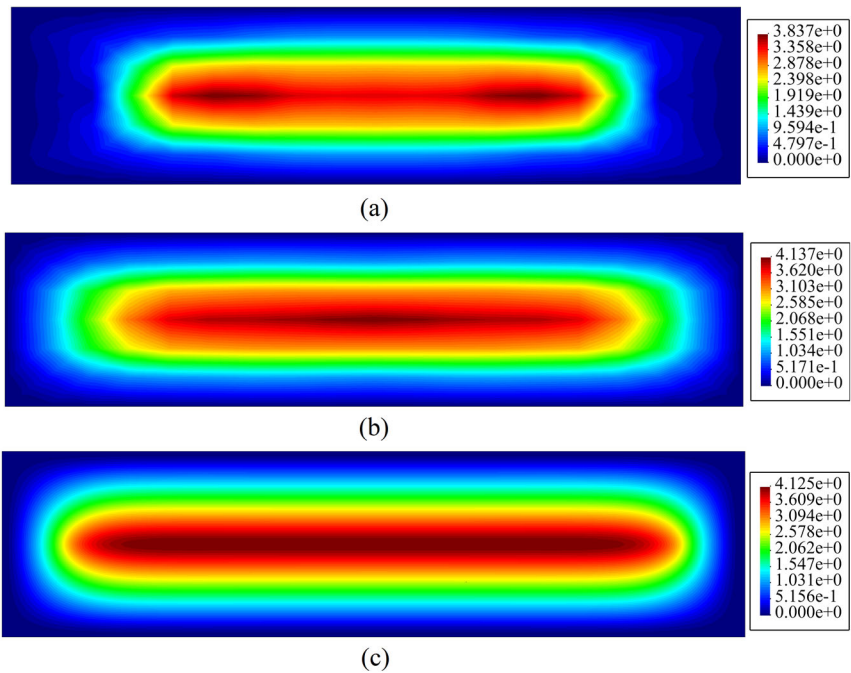
Fig. 26. Total displacement contours at time-step 13 obtained by (a) iFEM analysis using discrete sensors, (b) iFEM analysis using polynomial smoothing approach, and (c) FEM analysis.

Finally, the three-dimensional deformed shapes reconstructed utilizing the iQS4 models of the iFEM (discrete and pre-extrapolated strains) are compared with each other and reference solutions in Fig. 27. According to these deformed shapes, the improved performance of iFEM-iQS4 with pre-extrapolated strains can be observed for full-field large deformation sensing, thus proving the experimental advantages of the proposed method. Overall, this study case experimentally verifies the ability of the iFEM-iQS4 inverse element to capture the geometrically non-linear deflection of thin laminates and validates the practical utility of the strain pre-extrapolation technique for the iFEM-FSDT approach. The computational strategy presented here can be used to develop accurate and efficient applications of the iFEM-FSDT method in future research on shape detection of thin laminated structures subjected to large deformations using a small number of discrete sensors.
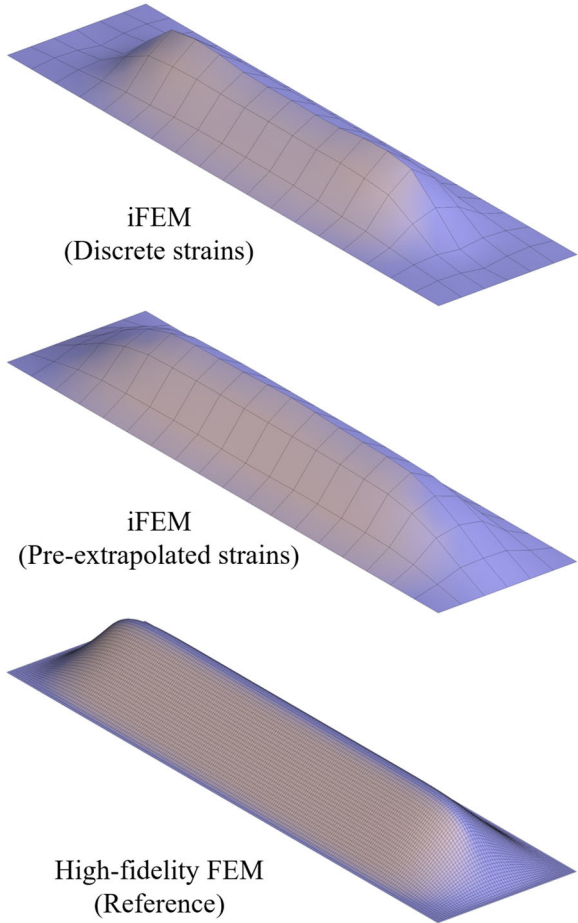
Fig. 27. Comparison of three-dimensional deformed shapes (30 times magnified) obtained at time-step 13.

4. Conclusion

This study presents an experimental and numerical evaluation for shape sensing of thin laminated structures subjected to large deformations using the iFEM approach. The iFEM is a sensor-based algorithm that uses a weighted least squares function to minimize the error between experimental and numerical section strains to predict full-field deformations. To this end, the entire domain of the structure is discretized into quadrilateral inverse shell elements, referred to as the iFEM-iQS4 model. For the numerical verification of the iFEM approach for geometrically non-linear displacement monitoring of thin laminated structures, two case studies are considered, including a post-buckling analysis of a thin laminated plate and a curved thin laminated shell geometry subjected to large deformations. For this purpose, three different sensor placement models are used for these laminates.

Furthermore, the efficiency of the iFEM-iQS4 element is verified through experiments where initially a thin laminate is fabricated, and then the mechanical properties of the laminate are measured through tensile and shear tests. Moreover, this thin laminate is clamped on a fixture and then tested under large deflection deformation. The appropriate locations for installing sixteen strain rosettes are calculated to obtain the required strain data for the iFEM analysis. Then, these sensors are placed at the designated locations on the surface of the plate, and the strain data is collected using data acquisition systems. Since the sensors are discretely distributed from each other, the iFEM formulation is coupled with a strain data smoothing technique known as the "strain pre-extrapolation technique" to recover these sparse strain data over the entire area of the structure. This smoothing method also helps to neglect strain measurement errors and other operational mistakes during the analyses.

The obtained quantitative and qualitative results of the post-buckling analysis clearly show the high performance and accuracy of iFEM in buckling deformation reconstruction of thin laminates even by employing a few sensors. Moreover, the incremental iFEM analyses obtained for the curved shell laminate show a good agreement with the reference FEM solution by using sparse sensor deployments. In the experimental analyses, the efficiency of the coupled iFEM method with the pre-extrapolated strain technique is well demonstrated in recovering discrete strain data over the entire domain of the structure. This smoothed strain data leads to almost excellent reconstruction of the displacement field of the thin laminates subjected to large deformation. In

37

conclusion, the knowledge acquired from this study can be utilized as a practical guideline for future applications of the iFEM-iQS4 algorithm for displacement monitoring of thin laminated structural components subjected to geometrically non-linear deformations.

Acknowledgement

References

[1]   Oñate, E., 2013. Structural analysis with the finite element method. Linear statics: volume 2: beams, plates and shells. Springer Science & Business Media.

[2]   Chen, S., Huang, Y., Gu, P. and Wang, J.Y., 2019. Experimental study on fatigue performance of UHPC-orthotropic steel composite deck. Thin-Walled Structures, 142, pp.1-18.

[3]   Jiang, Z., Wan, S., Fang, Z. and Song, A., 2021. Static and fatigue behaviours of a bolted GFRP/steel double lap joint. Thin-Walled Structures, 158, p.107170.

[4]   Sheta, A., Ma, X., Zhuge, Y., ElGawady, M.A., Mills, J.E., Singh, A. and Abd-Elaal, E.S., 2021. Structural performance of novel thin-walled composite cold-formed steel/PE-ECC beams. Thin-Walled Structures, 162, p.107586.

[5]   Dar, M.A., Subramanian, N., Anbarasu, M., Ghowsi, A.F., Arif, P.A. and Dar, A.R., 2021. Testing and FE simulation of lightweight CFS composite built-up columns: Axial strength and deformation behaviour. Thin-Walled Structures, 167, p.108222.

[6]   Kootsookos, A. and Burchill, P.J., 2004. The effect of the degree of cure on the corrosion resistance of vinyl ester/glass fibre composites. Composites Part A: Applied Science and Manufacturing, 35(4), pp.501-508.

[7]   Diamanti, K. and Soutis, C., 2010. Structural health monitoring techniques for aircraft composite structures. Progress in Aerospace Sciences, 46(8), pp.342-352.

[8]   Yuan, S., Wang, L. and Peng, G., 2005. Neural network method based on a new damage signature for structural health monitoring. Thin-Walled Structures, 43(4), pp.553-563.

[9]   Güemes, A., Fernandez-Lopez, A., Pozo, A.R. and Sierra-Pérez, J., 2020. Structural health monitoring for advanced composite structures: a review. Journal of Composites Science, 4(1), p.13.

[10]   Van Driessche, A., Aggelis, D.G. and Tsangouri, E., 2021. Complex fracture on thin-wall textile reinforced cement (TRC) shells monitored by acoustic emission. Thin-Walled Structures, 167, p.108216.

[11] Gherlone, M., Cerracchio, P., Mattone, M., Di Sciuva, M. and Tessler, A., 2014. An inverse finite element method for beam shape sensing: theoretical framework and experimental validation. Smart Materials and Structures, 23(4), p.045027.

[12] Luyckx, G., Voet, E., Lammens, N. and Degrieck, J., 2011. Strain measurements of composite laminates with embedded fibre Bragg gratings: Criticism and opportunities for research. Sensors, 11(1), pp.384-408.

[13] Zanjani, J.S.M., Al-Nadhari, A.S. and Yildiz, M., 2018. Manufacturing of electroactive morphing carbon fiber/glass fiber/epoxy composite: process and structural monitoring by FBG sensors. Thin-Walled Structures, 130, pp.458-466.

[14] Zanjani, J.S.M., Louyeh, P.Y., Tabrizi, I.E., Al-Nadhari, A.S. and Yildiz, M., 2021. Thermo-responsive and shape-morphing CF/GF composite skin: Full-field experimental measurement, theoretical prediction, and finite element analysis. Thin-Walled Structures, 160, p.106874.

[15] Haltmeier, M. and Nguyen, L.V., 2020. Regularization of inverse problems by neural networks. arXiv preprint arXiv:2006.03972.

[16] Papadopoulos, V., Soimiris, G., Giovanis, D.G. and Papadrakakis, M., 2018. A neural network-based surrogate model for carbon nanotubes with geometric nonlinearities. Computer Methods in Applied Mechanics and Engineering, 328, pp.411-430.

[17] Davis, M.A., Kersey, A.D., Sirkis, J. and Friebele, E.J., 1996. Shape and vibration mode sensing using a fiber optic Bragg grating array. Smart Materials and Structures, 5(6), p.759.

[18] Bogert, P., Haugse, E. and Gehrki, R., 2003, April. Structural shape identification from experimental strains using a modal transformation technique. In 44th AIAA/ASME/ASCE/AHS/ASC Structures, Structural Dynamics, and Materials Conference (p. 1626).

[19] Kang, L.H., Kim, D.K. and Han, J.H., 2007. Estimation of dynamic structural displacements using fiber Bragg grating strain sensors. Journal of Sound and Vibration, 305(3), pp.534-542.

[20] Ko, W.L., Richards, W.L. and Fleischer, V.T., 2009. Applications of Ko displacement theory to the deformed shape predictions of the doubly tapered Ikhana Wing. NASA/TP-2009-214652.

[21] Kim, N.S. and Cho, N.S., 2004. Estimating deflection of a simple beam model using fiber optic Bragg-grating sensors. Experimental Mechanics, 44(4), pp.433-439.

[22] Tessler, A., and Spangler, J. L., 2003. A variational principal for reconstruction of elastic deformation of shear deformable plates and shells. NASA TM-2003-212445.

[23] Tessler, A. and Spangler, J.L., 2005. A least-squares variational method for full-field reconstruction of elastic deformations in shear-deformable plates and shells. Computer Methods in Applied Mechanics and Engineering, 194(2-5), pp.327-339.

[24] Gherlone, M., Cerracchio, P., Mattone, M., Di Sciuva, M. and Tessler, A., 2012. Shape sensing of 3D frame structures using an inverse finite element method. International Journal of Solids and Structures, 49(22), pp. 3100-3112.

[25] Savino, P., Tondolo, F., Gherlone, M. and Tessler, A., 2020. Application of Inverse Finite Element Method to Shape Sensing of Curved Beams. Sensors, 20(24), p.7012.

[26] Tessler, A., and Spangler, J. L., 2004. Inverse FEM for full-field reconstruction of elastic deformations in shear deformable plates and shells. In Proceedings of 2nd European Workshop on Structural Health Monitoring, Munich, Germany.

[27] Kefal, A., Oterkus, E., Tessler, A. and Spangler, J.L., 2016. A quadrilateral inverse-shell element with drilling degrees of freedom for shape sensing and structural health monitoring. Engineering Science and Technology, an International Journal, 19(3), pp.1299-1313.

[28] Kefal, A., 2019. An efficient curved inverse-shell element for shape sensing and structural health monitoring of cylindrical marine structures. Ocean Engineering, 188, p.106262.

[29] Abdollahzadeh, M.A., Kefal, A. and Yildiz, M., 2020. A comparative and review study on shape and stress sensing of flat/curved shell geometries using C0-continuous family of iFEM elements. Sensors, 20(14), p.3808.

[30] Kefal, A. and Oterkus, E., 2016. Displacement and stress monitoring of a Panamax containership using inverse finite element method. Ocean Engineering, 119, pp.16-29.

[31] Kefal, A. and Oterkus, E., 2016. Displacement and stress monitoring of a chemical tanker based on inverse finite element method. Ocean Engineering, 112, pp.33-46.

[32] Kefal, A., Mayang, J.B., Oterkus, E. and Yildiz, M., 2018. Three-dimensional shape and stress monitoring of bulk carriers based on iFEM methodology. Ocean Engineering, 147, pp.256-267.

[33] Li, M., Kefal, A., Oterkus, E. and Oterkus, S., 2020. Structural health monitoring of an offshore wind turbine tower using iFEM methodology. Ocean Engineering, 204, p.107291.

[34] Abdollahzadeh, M.A., Yildiz, M. and Kefal, A., Three-Dimensional Shape Sensing of a Representative Ship-Hull Cross-Section Based on Inverse Finite Element Method. In 34th Asian-Pacific Technical Exchange and Advisory Meetings on Marine Structures, Istanbul, Turkey.

[35] Esposito, M. and Gherlone, M., 2020. Composite wing box deformed-shape reconstruction based on measured strains: Optimization and comparison of existing approaches. Aerospace Science and Technology, 99, p.105758.

[36] Oboe, D., Colombo, L., Sbarufatti, C. and Giglio, M., 2021. Shape Sensing of a Complex Aeronautical Structure with Inverse Finite Element Method. Sensors, 21(4), p.1388.

[37] Papa, U., Russo, S., Lamboglia, A., Del Core, G. and Iannuzzo, G., 2017. Health structure monitoring for the design of an innovative UAS fixed wing through inverse finite element method (iFEM). Aerospace Science and Technology, 69, pp.439-448.

[38] Esposito, M. and Gherlone, M., 2021. Material and strain sensing uncertainties quantification for the shape sensing of a composite wing box. Mechanical Systems and Signal Processing, 160, p.107875.

[39] You, R., Ren, L., Yuan, C. and Song, G., 2021. Two-Dimensional Deformation Estimation of Beam-Like Structures Using Inverse Finite-Element Method: Theoretical Study and Experimental Validation. Journal of Engineering Mechanics, 147(5), p.04021019.

[40] You, R. and Ren, L., 2021. An enhanced inverse beam element for shape estimation of beam-like structures. Measurement, 181, p.109575.

[41] Xu, H., Zhou, Q., Yang, L., Liu, M., Gao, D., Wu, Z. and Cao, M., 2020. Reconstruction of full-field complex deformed shapes of thin-walled special-section beam structures based on in situ strain measurement. Advances in Structural Engineering, 23(15), pp.3335-3350.

[42] Zhao, F., Bao, H., Xue, S. and Xu, Q., 2019. Multi-objective particle swarm optimization of sensor distribution scheme with consideration of the accuracy and the robustness for deformation reconstruction. Sensors, 19(6), p.1306.

[43] Zhao, Y., Du, J., Bao, H. and Xu, Q., 2018. Optimal sensor placement for inverse finite element reconstruction of three-dimensional frame deformation. International Journal of Aerospace Engineering, 2018.

[44] Ghasemzadeh, M. and Kefal, A., Optimization of Sensor Placement for Stiffened Marine Panels Using Coupled Genetic Algorithm, and Inverse Finite Element Method. In 34th Asian-Pacific Technical Exchange and Advisory Meetings on Marine Structures, Istanbul, Turkey.

[45] Kefal, A. and Oterkus, E., 2017. Shape Sensing of Aerospace Structures by Coupling Isogeometric Analysis and Inverse Finite Element Method. In 58th AIAA/ASCE/AHS/ASC Structures, Structural Dynamics, and Materials Conference (p. 0427).

[46] Kefal, A. and Oterkus, E., 2020. Isogeometric iFEM analysis of thin shell structures. Sensors, 20(9), p.2685.

[47] Zhao, F., Xu, L., Bao, H. and Du, J., 2020. Shape sensing of variable cross-section beam using the inverse finite element method and isogeometric analysis. Measurement, 158, p.107656.

[48] Zhao, F. and Bao, H., 2021. An improved inverse finite element method for shape sensing using isogeometric analysis. Measurement, 167, p.108282.

[49] Kefal, A., Diyaroglu, C., Yildiz, M. and Oterkus, E., 2021. Coupling of peridynamics and inverse finite element method for shape sensing and crack propagation monitoring of plate structures. Computer Methods in Applied Mechanics and Engineering.

[50] Tessler, A., Roy, R., Esposito, M., Surace, C. and Gherlone, M., 2018. Shape sensing of plate and shell structures undergoing large displacements using the inverse finite element method. Shock and Vibration, Article ID 8076085.

[51] Cerracchio, P., Gherlone, M., Di Sciuva, M. and Tessler, A., 2015. A novel approach for displacement and stress monitoring of sandwich structures based on the inverse finite element method. Composite Structures, 127, pp.69-76.

[52] Kefal, A., Tessler, A. and Oterkus, E., 2017. An enhanced inverse finite element method for displacement and stress monitoring of multilayered composite and sandwich structures. Composite Structures, 179, pp.514-540.

[53] Tessler, A., Di Sciuva, M. and Gherlone, M., 2010. A consistent refinement of first-order shear deformation theory for laminated composite and sandwich plates using improved zigzag kinematics. Journal of Mechanics of Materials and Structures, 5(2), pp.341-367.

[54] Kefal, A., Tabrizi, I.E., Yildiz, M. and Tessler, A., 2021. A smoothed iFEM approach for efficient shape-sensing applications: Numerical and experimental validation on composite structures. Mechanical Systems and Signal Processing, 152, p.107486.

[55] Kefal, A., Tabrizi, I.E., Tansan, M., Kisa, E. and Yildiz, M., 2021. An experimental implementation of inverse finite element method for real-time shape and strain sensing of composite and sandwich structures. Composite Structures, 258, p.113431.

[56] Abdollahzadeh, M.A., Tabrizi, I.E., Kefal, A. and Yildiz, M., 2021. A Combined Experimental/Numerical Study on Deformation Sensing of Sandwich Structures through Inverse Analysis of Pre-Extrapolated Strain Measurements. Measurement, p.110031.

[57] Cerracchio, P., Gherlone, M. and Tessler, A., 2015. Real-time displacement monitoring of a composite stiffened panel subjected to mechanical and thermal loads. Meccanica, 50(10), pp.2487-2496.

[58] Oboe, D., Colombo, L., Sbarufatti, C. and Giglio, M., 2021. Comparison of strain pre-extrapolation techniques for shape and strain sensing by iFEM of a composite plate subjected to compression buckling. Composite Structures, 262, p.113587.

[59] Colombo, L., Oboe, D., Sbarufatti, C., Cadini, F., Russo, S. and Giglio, M., 2021. Shape sensing and damage identification with iFEM on a composite structure subjected to impact damage and non-trivial boundary conditions. Mechanical Systems and Signal Processing, 148, p.107163.

[60] Hughes, T.J. and Brezzi, F., 1989. On drilling degrees of freedom. Computer methods in applied mechanics and engineering, 72(1), pp.105-121.

[61] Tessler, A. and Hughes, T.J., 1983. An improved treatment of transverse shear in the Mindlin-type four-node quadrilateral element. Computer methods in applied mechanics and engineering, 39(3), pp.311-335.

[62] Tessler, A., Riggs, H. R., and Dambach, M., 1999. A novel four-node quadrilateral smoothing element for stress enhancement and error estimation. International Journal for Numerical Methods in Engineering, 44(10), pp. 1527-1541

[63] Tessler, A., Riggs, H. R., Freese, C. E., and Cook, G. M., 1998. An improved variational method for finite element stress recovery and a posteriori error estimation. Computer Methods in Applied Mechanics and Engineering, 155(1), pp. 15-30.

[64] Stolarski, T., Nakasone, Y. and Yoshimoto, S., 2018. Engineering analysis with ANSYS software. Butterworth-Heinemann.

[65] Kreja, I. and Schmidt, R., 2006. Large rotations in first-order shear deformation FE analysis of laminated shells. International Journal of Non-Linear Mechanics, 41(1), pp.101-123.